Università degli Studi di Padova
Facoltà di Ingegneria

Dipartimento di Ingegneria dell'Informazione
Tesi di Laurea in Bioingegneria

Quantification of lung glucose metabolism with positron emission tomography in patients with Acute Lung Injury

Relatore: Ch.ma Prof.ssa Alessandra Bertoldo
Correlatori: Prof.ssa Rosa Maria Moresco
Ing. Mattia Veronese

Laureanda: Elisabetta Grecchi

Anno Accademico 2010-2011

Contents

List of Figures

List of Tables

Introduction

Acute lung injury (ALI) and its severe form, acute respiratory distress syndrome (ARDS), are lung pathologies that confer considerable morbidity and high mortality. They usually occur short after an ordinary injury (e.g. trauma, burns, aspiration) or an acute illness (e.g. pneumonia, acute pancreatitis).
Acute lung injury has no specific treatment but it is common practice to treat it with mechanical ventilation in supportive care in order to reduce airway pressure while maintaining adequate oxygenation. Ventilation is usually provided through oro-tracheal tube or tracheostomy.

Studies hve demonstrated that one cause of ALI exacerbation to ARDS can be the mechanical ventilation provided in the intensive care unit ICU because high airway pressures applied to both healthy and injured lungs can aggravate inflammation by promoting alveolar distention. The physiological processes that are behind this evolution are not completely clear. Probably they are correlated to polymorphonuclear neutrophils (PMNs) activation, that is the mainstay of inflammation. However the uncertainty about the dynamic of the system justifies an onward interest in studying lung inflammation.

Positron Emission Tomography (PET) with $[^{18}F]$-fluoro-2-deoxy-D-glucose (FDG) tracer is a nuclear medicine imaging technique that produces three-dimensional pictures of the functional processes of the model related to tissue metabolic activity. The data resulting from FDG-PET studies *in vivo* are already widely used to extract quantitative and qualitatively clinical information like the metabolic rate, the blood flow in the brain, the receptor affinity of drugs in cerebral structures, etc. Since neutrophils activation is

associated to an increase in cellular metabolism, FDG-PET studies could be suitable to describe the dynamic of lung inflammation.

In this work we performed FDG-PET studies on a dataset composed by 17 subjects with the aim of quantifying the dynamic of the glucose metabolism in healthy and injured lung tissues. Twelve subjects were patients affected by a severe form of ALI undergoing mechanical ventilation. Five subjects were healthy volunteer, whose studies were used as control.

Image pre-processing of the data was necessary in order to distinguish the lung from the other tissues present in the thoracic area, to define the regions of interest (ROIs) and to reconstruct the arterial input function. These operations were performed using both PET and CT data. The graphical method (Patlak plot) and the data-driven methods (spectral analysis and spectral analysis iterative filter) were then applied to quantify glucose metabolism. Analyses were carried out at both ROI and voxel level. With this double level analysis it has been possible to consider the presence of heterogeneity in the lung tissues. The results of quantification suggested that the presence of inflammation in the lung tissues greatly affects the metabolism of glucose compared to the healthy subjects. Moreover the application of the FDG-PET method allowed a better classification of the level of inflammation in injured lungs than the standard approach based on CT. Even though more studies are still necessary to define a full-model of the glucose metabolism system in lungs; the application of Spectral Analysis methodologies gave important indications about the number of compartments necessary to describe the data at both ROI and voxel level.

Chapter 1

Clinical Overview

1.1 Positron Emission Tomography

Positron emission tomography (PET) has made it possible to detect accurately and noninvasively at the regional level (i.e., organ and tissue) the concentration of radiopharmaceuticals tagged with positron emitters. Image analysis can be made both qualitatively and quantitatively. For some clinical PET studies, a qualitative analysis is appropriate to answer biological questions, such as when the localization of metabolic defects is the principal purpose of the study. However, quantitative information is often necessary, and this requires interpretation of the PET tracer measurement with a mathematical model of the underlying physiological process. PET kinetic modeling allows, for example, the estimation of the glucose metabolic rate and blood flow in the brain (Phelps 1979; Iida 1986), in the skeletal muscle (Kelley 1999a; Kelley 1996; Ruotsalainen 1997), and in myocardium (Gambhir 1989; Bergman 1984), as well as estimation of receptor affinity in specific cerebral structures (Wong 1986). Recently it has been used also for lung regional metabolic activity quantification during inflammation (Schroeder 2008; Bellani 2009) to enable a better understanding of inflammatory processes at all stages of disease.[5]

1.1.1 Principles

Positron Emission Tomography is a nuclear imaging modality that excels in depicting the biology of living tissue and that enables regional function to be assayed in a fully quantitative and noninvasive manner. While the resolution of magnetic resonance imaging (MRI) for structural tissue changes is unsurpassed, the ability of structural MRI to demonstrate alterations in the physiology and metabolic function of tissues remains poor. For this reason, combining the functional PET data with the high-resolution anatomical maps produced by MRI provides powerful data sets which allow correspondences to be identified and analyze in a better way the different structures [4]. This combination of techniques is recommended especially for the brain, as in our study, since it is a complex neuronal network in which all subunits can communicate directly or indirectly with each other. This nuclear technique involves the introduction, usually via an intravenous injection, of a radioactive tracer into the human body; they are prepared in a cyclotron that accelerates a beam of protons and directs it towards the target nuclei, thereby incorporating an extra proton into them: this generates new compounds that are energetically unstable. The isotopes are then coupled to the compound of interest and that is the tracer. Since they are unstable, the isotopes undergo a process of decay whereby the excess proton is converted into a neutron, a positron, and a neutrino: the emitted positron travels up to a range of a few millimeters in tissue before annihilates with an electron [15] (Figure 1.1.1(a)). This mutual annihilation process produces two 511 keV rays going in opposite directions (they are released at 180) and which are detected by the several rings of PET scanner. This consists of circumferential arrays of detectors which look for coincidence events, in which two ray interaction occur almost simultaneously on opposite side of the head (Figure 1.1.1(b)). Finally, through reconstruction software the tomographic image is obtained: the count density in the resulting images, assuming appropriate data corrections are applied, reflects the concentration of the positron-emitting isotope in the tissue. The main characteristics that make PET a charming technique in the neuroimaging field are superior sensi-

tivity, high quantity of information and a greater flexibility of incorporating positron labels into biomolecules. On the other side, the main disadvantage of PET is greater expense in comparison with other techniques.

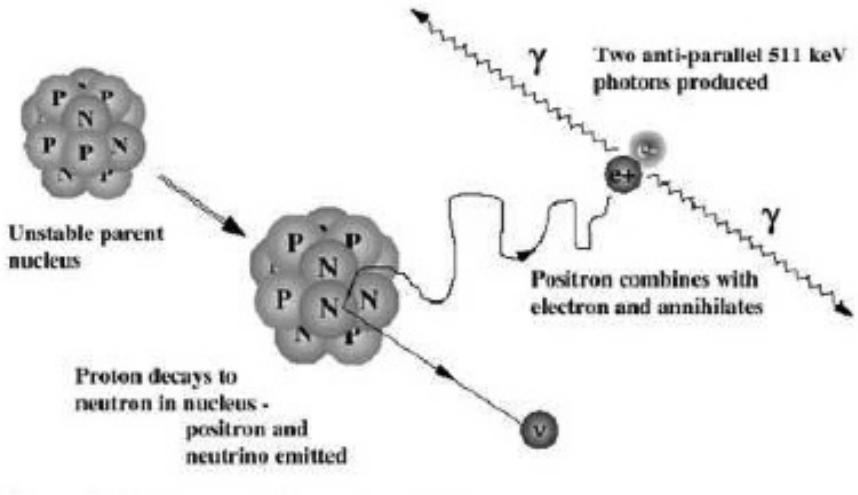

(a) Positron emission and annihilation

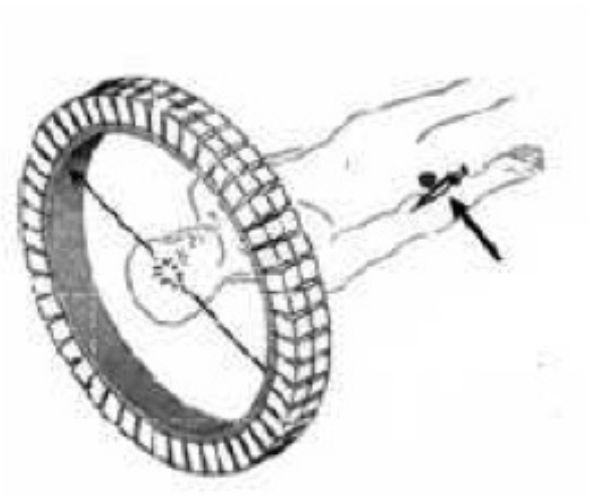

(b) Schematic representation of detectors in PET

Figure 1.1: The main principles of PET imaging.

1.1.2 Tracers

A tracer is an indicator molecule that follows a systemic substance that might be involved in flow, metabolism or drug-binding process and that is labelled with a positron–emitting isotope. It should be analogous to the systemic substance and does not perturb the system. Availability of carbon, oxygen and nitrogen isotopes makes easy to study biological processes with PET because these are elements present in almost all organic molecules.

Isotope	Half-Live	Tracer	Parameters
Nitrogen-13 ^{13}N	9.8 min	Ammonia	Coronary flow
Carbon-11 ^{11}C	20.4 min	Palmitate	Fatty acid metabolism
		Acetate	Oxygen consumption
Fluorine-18 ^{18}F	109.8 min	Fludeoxyglucose	Glucose metabolism
Oxygen-15 ^{15}O	2.07 min	Water	Local fluxes
		Carbon dioxide	Local fluxes
		Carbon monoxide	Blood volume
Rubidium 82 ^{82}Rb	4.58 hours	Rubidium	Miocardic perfusion

Table 1.1: Labelled molecules used in PET tracers.

Looking at the table, it is noticeable the relatively short half-lives of tracers. This implies two advantages. First, it is possible to employ high radioactivity, that results in a quite accurate measurement without exposing the subjects to prolonged periods of radiation; second, several studies on the same patient are possible in a reasonable time interval.[6]

1.2 Lung disease

1.2.1 Definition and Histopathology

Acute lung injury (ALI) and acute respiratory distress syndrome (ARDS) are characterized by the abrupt onset of clinically significant respiratory failure with presence of diffuse pulmonary infiltrates. They are shown on radiograph as pulmonary edema resulting from increased pulmonary vascular

permeability, with alveolar flooding and loss of compliance. Both pathologies can be the consequence of pulmonary or extra pulmonary insults but the likelihood of developing depends on the predisposing disorder, some events are more likely to progress to lung injury than others. The pulmonary inflammation response is a complex process involving a number of different cell types some of which, that usually play an important role in counter infection and heal lung tissue, may be themselves partially responsible for the pathogenesis of chronic lung disease that leads to irreversible lung damage and loss of function.

ALI is characterized by hypoxaemia (PaO2/FiO2 ratio $<$ 300 mm Hg) [1] without an excessive increase in pulmonary capillary pressure; when the hypoxaemia is severe (PaO2/FiO2 $<$ 200 mm Hg) disorder is termed as acute respiratory distress syndrome (ARDS). However, most epidemiological and interventional studies use the broader range of gas exchange abnormality and refer to the overall disorder as acute lung injury; these definitions have limitations due to variability of several physiological parameters. Hypoxaemia is a clinically manifestation of the early phase of inflammation where leakage of edema fluid into the lung and inflammatory cellular infiltration cause diffusion abnormalities and ventilation perfusion mismatch.[8]

Increased alveolar capillary membrane permeability is a central feature of the acute phase of ALI and ARDS. It is associated with diffuse alveolar damage, which includes alveolar flooding, infiltration by neutrophils and macrophages, and formation of hyaline membranes.

Early acute lung injury is histologically characterized by a diffuse neutrophilic alveolar infiltrate and the accumulation of a protein-rich pulmonary edema. During this acute phase, cytokines incite and perpetuate inflammation. By increasing oxidant stress and protease activity, the inflammatory mixture in the alveoli and interstitium reduces surfactant production, and inactivates remaining surfactant, thereby promoting widespread atelectasis. Additionally, there is a damage of the structural framework of the lung, and both alveolar capillary and epithelial-cell injury can be seen. Damage of

[1] *PaO2* is the partial pressure of oxygen while *FiO2* is the fraction of inspired oxygen. Ratio indicates the effectiveness of oxygen transition through alveolus-capillary membrane

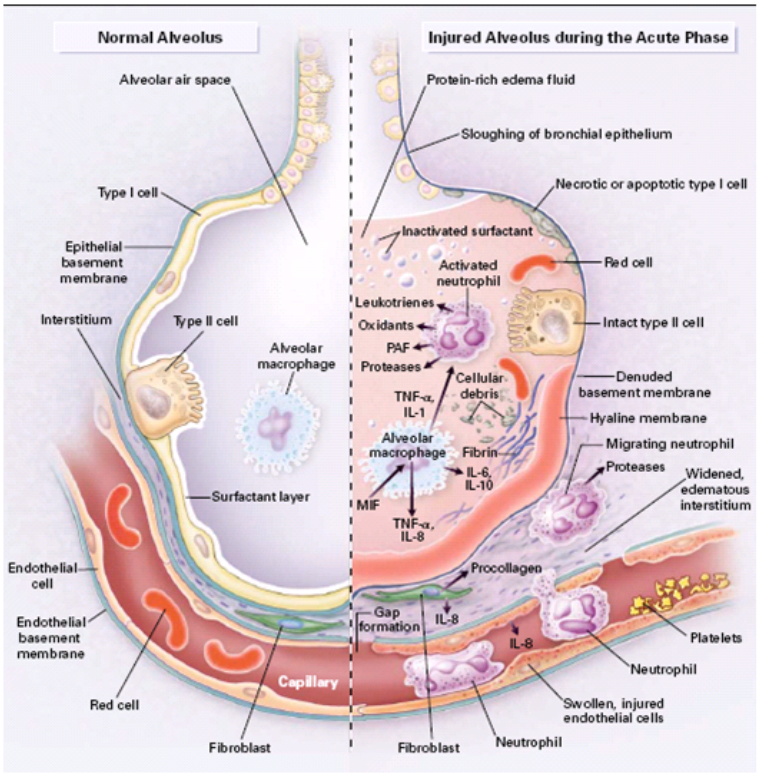

Figure 1.2: Normal and inflamed alveolus.

the epithelial barrier exacerbates the tendency for alveolar flooding, and delays recovery by impairing fluid clearance. The inflammatory process can evolve to a subacute phase characterized by fibroproliferation. Depending on the balance between fibroproliferation and alveolar repair, some patients recover without sequelae, but others experience pulmonary fibrosis and chronic respiratory failure. Neutrophils become highly activated in response to inflammatory stimuli and they are key modulators of the magnitude of injury during ALI and ARDS.[20]

The scenario where this phenomena takes place is represented by a "wet" lung with alveolar instability and areas which collapse, leaving little room for ventilation. The alveoli of the remaining "baby lung"[2], which has to receive the entire minute ventilation, will be abnormally stretched and overdistended,

[2] "baby lung" is that part of the lung that keeps normal aeration. The shape of this part reminds the one of a normal lung but with smaller size; that is why it is so called "baby lung"

particularly if the tidal volume is not properly reduced.[8][2][9]

1.2.2 FDG-PET: evaluation of lung inflammation

FDG PET imaging technique allows to quantify tissue glucose metabolism in vivo in human; for this it could be a good investigation method also because noninvasive and accurate quantification of pulmonary inflammation throughout the lung could be obtained. As already mentioned neutrophilis become highly activated during ALI and for this reason they are key modulators of the magnitude of injury. They rely on anaerobic glycolysis for energy production and consume 20-30 times more glucose when activated than the rest. In order to avoid artifacts due to glucose metabolite FDG is preferably used instead.

FDG is a glucose analogue used as a marker of metabolism because it is carried into cells by the same transporter proteins as glucose. Once there, in the presence of hexokinase, it is phosphorylated to [^{18}F]FDG-6-phosphate, which unlike glucose-6-phosphate cannot be further metabolized via the Krebs cycle. In tissues with low dephosphorylase activity (such as lung, brain, and heart), dephosphorylation has been found to be negligible for at least 1 hour after FDG injection, therefore it is considered trapped intracellularly. Understanding of the factors determining FDG uptake is crucial for an adequate signal interpretation and for the introduction of FDG PET to clinical use. The current concept, easy to guess, is that the FDG imaging signal during ALI is predominantly determined by the combination of the absolute number of neutrophils in the field of view and their state of activation. Even though, Prost et. al. [8] found in a sheep-model of alverolar lavage that an increase in lung water can generate an additional volume of distribution of FDG. This volume is not a precursor for phosphorylation and can artifactually increase lung FDG uptake independently of lung inflammation.

In this work we applied FDG quantification method to study lung glucose metabolism in 5 healthy subjects and 12 patients affected with ALI/ARDS at different stages.

Chapter 2

Data acquisition and pre-processing

In this section we are going to explain how clinical tests have been conducted and how data have been pre–processed before actual FDG metabolism quantification.

2.1 Subjects and investigational protocol

The protocol was approved by the institution's ethical committee; informed consent was obtained according to the committee's recommendations. Patients were recruited from the general Intensive Care Unit (ICU) of HSR university hospital.

Inclusion criteria were:

- diagnosis of ALI/ARDS, with a positive end-expiratory pressure (PEEP) of at least 8 cm H2O, according to the 1994 European/American Consensus conference , requiring mechanical ventilation
- planning by the attending physician of a thorax CT scan as part of the patient's clinical management

Exclusion criteria were:

- pregnancy
- age < 18 years
- impossibility of patient's transport according to the attending physician
- lung surgery in the previous four weeks to the PET exam
- oliguria (urinary output <0.5 ml/kg/hour) or anuria
- known or suspected cancer
- history of chronic lung disease
- logistical reasons (e.g. PET/CT camera unavailable until patient had lost eligibility criteria)

Once a patient was judged eligible for the study, the PET/CT scan was scheduled, usually within one or two days; on the day of the study eligibility was confirmed. The enteral or parenteral nutrition and any glucose-containing infusion were stopped at 6 a.m. to ensure a fasting period of at least 6-8 hours. In patients undergoing insulin therapy, this was stopped as well and before transport to PET/CT facility, blood glucose was tested to confirm a level between 80 and 140 mg/dl because altered glucose level could affect test results. The PET/CT study being usually performed around 2 p.m. Before transport from the ICU to the PET/CT facility, arterial blood gases and hemodynamic and respiratory parameters have been recorded. During transport, and throughout the permanence in the PET/CT facility, clinical care was provided by a physician and a nurse uninvolved in the study procedures. Mechanical ventilation was provided by an ICU ventilator, and invasive arterial blood pressure, ECG, peripheral oxygen saturation and expired CO2 were continuously monitored. Ventilatory settings, sedation, and fluid therapy were maintained constant throughout the study period, unless clinically advised. At the end of the study, collection of the aforementioned variables was repeated in the ICU. Finally, the 28 days and ICU outcome (survival or death) of each patient were recorded.[2][1]

2.2 Image Acquisition

Along with PET, computed tomography (CT) scans were also performed to obtain anatomical details.

It has been used a GE Discovery ST (GE Medical Systems, Milwaukee, WI) PET/CT tomograph, with an axial field of view of approximately 18 cm (47 3.27-mm thick sections, separated by 0.48 mm intervals), equipped with an 8-slice CT. The section of thorax to be imaged was selected on the scout view just above the diaphragm. A spiral CT scan (slice thickness 3.75 mm, no interval between slices) of the chosen section was obtained while holding the patient apneic (by switching the ventilator to Constant Positive Airway Pressure modality) at the same mean airway pressure as during mechanical ventilation, to ensure the best possible cross-registration between the CT scan and the PET acquisition to follow, performed during tidal ventilation. The patient was then advanced to the PET detector; the tomograph ensures the cross-registration of the same axial field-of-view between the CT and the PET acquisition. A bolus of ^{18}FDG (approximately 300 MBq) was rapidly injected intravenously, five seconds after that the acquisition of sequential PET frames was started with the following protocol: 12 frames lasting 10 seconds each (12frames x 10sec), 10frames x 30sec, 8frames x 300sec, 1frames x 600sec, for a total imaging time of 57 minutes. At the end of the PET scanning two additional sets of CT scans holding the airway pressure constant at the level of end- expiration (PEEP, CTEXP) and end-inspiration (Plateau pressure, CTINSP) were acquired to obtain images of the regional lung expansion induced by tidal ventilation.

2.3 Image Processing

Dynamic PET data were reconstructed by ordered-subset expectation maximization (OSEM) iterative algorithm and corrected for decay, scatter, random counts. Before quantification some operations are needed

1. Masking: lung tissue and aorta segmentation

2. Extraction of regions of interest

3. Extraction of input function from PET images

These elaborations have been made with a software specifically developed in Matlab environment (Matlab R2009b, The Mathworks, Natick, MA).

Data needed were extracted directly from noisy PET images; in order to obtain signal as thorough as possible, a precise ROI definition was needed.

2.3.1 Masking

Thoracic area is wide and heterogeneous so we need to define an area of interest to limit external contributions. We have to segment lung tissue, to quantify glucose metabolism, and aorta area to be able to extract input function.

Lung

Lung field (Region of interest, ROI_L) was manually outlined on the CT images, carefully avoiding the large airways, vessels and pleural effusion. Considering lung heterogeneity, a semi-automatic iterative algorithm has been implemented to be able to process aerated and not aerated regions and allow clinicians to choose lung tissue area.

First of all, a threshold value was required to discern between aerated (threshold 0.3) and not aerated (threshold 0.05-0.1) tissue then the user has to select a voxel on the CT image according to the threshold. The region was then iteratively grown by comparing all unallocated neighboring voxels to the region. The difference between a voxel's intensity value and the region's mean, was used as a measure of similarity. The voxel with the smallest difference measured this way was allocated to the respective region. This process stopped when the intensity difference between region mean and new voxel become larger than the selected threshold and an image of the selected area was shown near the CT image. The user could then decide to add other regions or go on analyzing other slices.

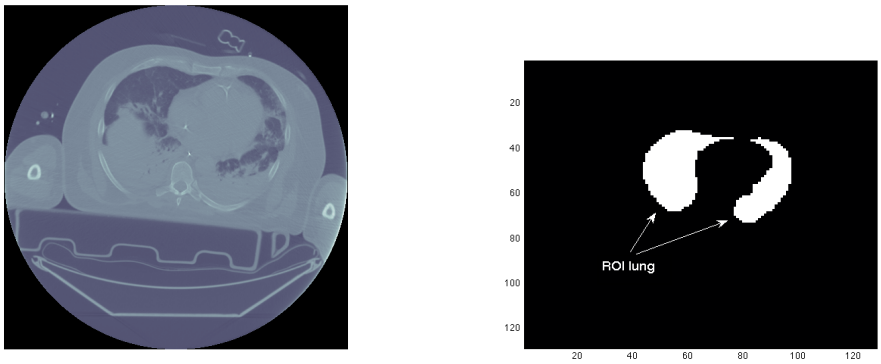

(a) Lung CT image (b) Mask of one the lung

Figure 2.1: Lung CT image in one representative subject and corresponding mask.

Aorta

Definition of aorta mask is less precise and rely more on clinician experience. Observing PET images at early time ROI, mask was defined approximately in the center of the descending aorta over few slices, selecting few voxel showing higher activity.

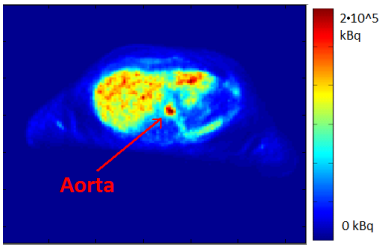

Figure 2.2: PET image of one representative subject showing aorta area.

2.3.2 Density based ROI

The original CT matrix, with a size of 512-by-512 voxels, was re-scaled to achieve the same dimension (128-by-128) and voxel size (4.5 mm) of the original PET image. This scaling process lowers the spatial resolution of CT to a level similar to PET. To select regions of interest we need to sub-segment

lung tissue previously defined with masking procedure. ROIs were defined on CT images following two configurations:

- original ROI_L was sub–segmented by allocating all the voxels within "bins" 100 Hounsfield Units (HU) wide (the first "submask" enclosed all the voxels between -1000 HU and -900 HU, the second comprised all the voxels between -900 HU and -800 HU, and so forth) in order to describe the intra-patient relationship between lung density and [^{18}F]FDG uptake.

- a segmentation ables to discern between inflamed tissue, with alveolar instability collapse, and the remaining healthy one, whose alveoli are overdistended to compensate for loss of functionality (draft on Figure 2.3). These two area (low density and high density) were defined as follows

  – Normally Aerated (NA): [-900 -501] Hounsfield Units (HU)

  – Collapsed or consolidated (CO): [-100 100] Hounsfield Units (HU)

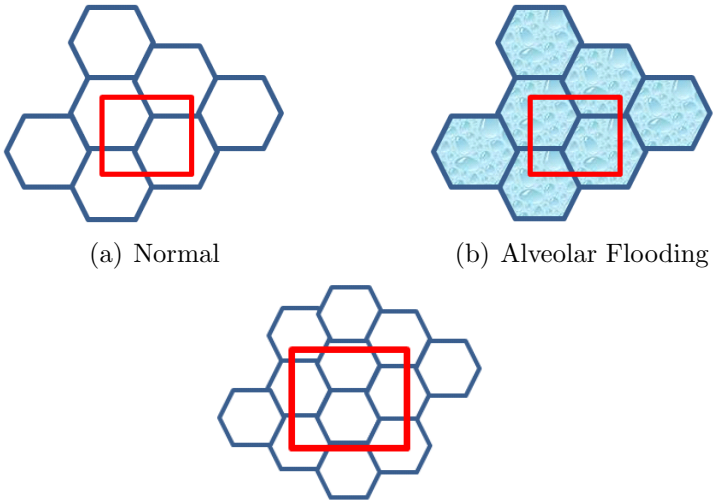

(a) Normal (b) Alveolar Flooding

(c) Alveolar Collapse

Figure 2.3: Different alveolar situation in ALI. The red box is an example of voxel area.

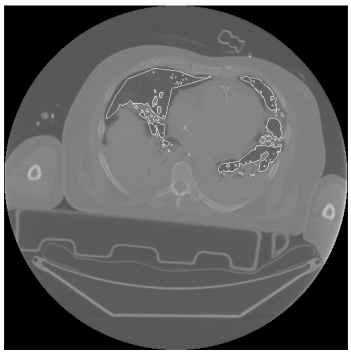

(a) Aerated region on CT image

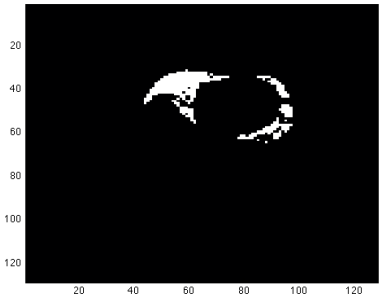

(b) Aerated region mask

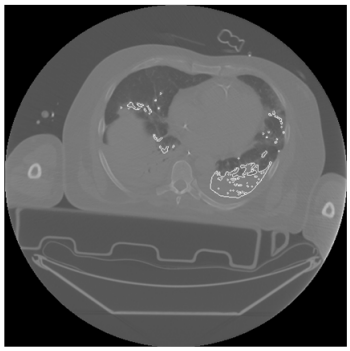

(c) Collapsed region on CT image

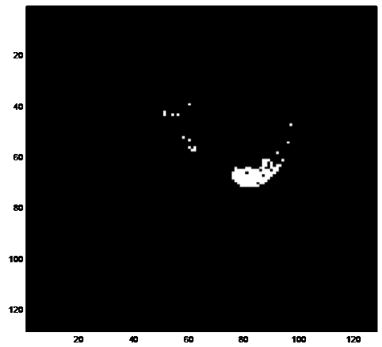

(d) Collapsed region mask

Figure 2.4: CT image in one representative subject and corresponding mask of both aerated and collapsed tissue.

2.3.3 Input function

Assessment of lung FDG kinetics implies knowledge of the time-activity curve in pulmonary artery plasma as an input function. Acquisition of this input function typically involves sequential arterial blood sampling, a process that is invasive and prone to measurement artifacts, exposes the clinical staff to radiation and blood, and adds costly laboratory procedures.

Literature provides methods to extract the input function; one of this is the *image defined* input function. Some conditions are required:

- individuation of a large arterial vessel
- partial volume and spillover correction
- absence or minor presence of metabolites.

We could apply this method because we defined the input function directly on the aorta, that is the biggest artery and limits partial volume and spillover contributions. As regards the third condition, FDG hasn't got metabolites so all conditions were fulfilled. In the current study after we had defined aorta region, aorta activity curves were collected and one third of these (the ones with the higher peaks) were taken into consideration to obtain the first part of the average blood signal (first minute, when the signal is higher). Signal was completed averaging the remaining two thirds of the collected curves. Operating this way, we could obtain a plasmatic activity curve with a high peak and a low "tail".

Tissue activity curves were easier to calculate because it was not necessary to obtain a high and well defined peak, but it was sufficient to simply average the activity of the ROI. In some cases, it has been necessary to shift the plasmatic curve to fit time-peak with the tissue one.

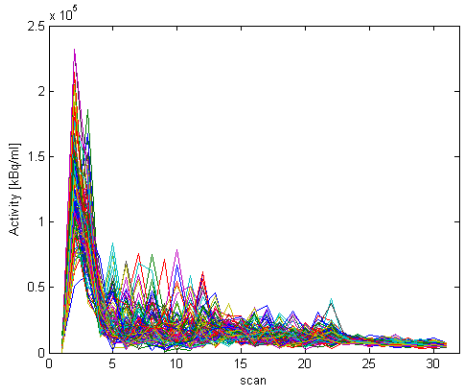

(a) Aorta activity curves in one representative subject

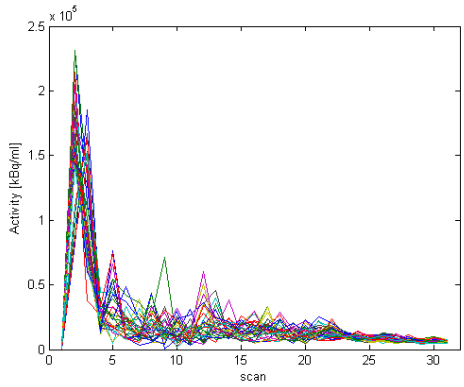

(b) One-third of total curves with higher peak

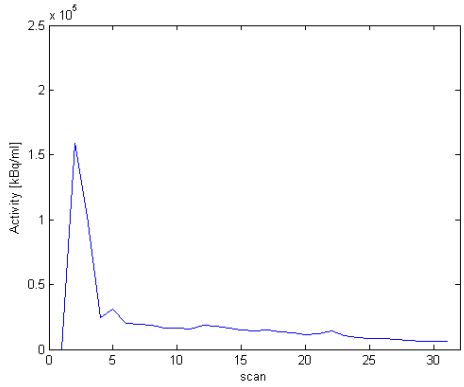

(c) Resulting input function

Figure 2.5: Steps to obtain input function from aorta activity curves in one representative subject.

Chapter 3

Modeling and physiological parameter quantification

Positron emission tomography makes possible a non invasive measurement and imaging of tracer concentration at regional level. Image analysis can be either qualitative, quantitative with opportune mathematical models or through visual inspection. In recent years several models and methods to convert radioactivity concentration into physiological parameters have been developed: compartmental (Sokoloff et. al., 1977), data–driven (Cunningham et al., 1993) and graphical (Patlak et. al., 1983) models.

Compartmental models are widely used in tracer kinetic studies; their purpose is to provide a quantitative description in terms of rate of effusion, transport and metabolism of a certain substance starting from tissue-time and plasma activity curves.

Data–driven methods are based on a black box estimation problem description. A very popular one is the so called Spectral Analysis, introduced by Cunningham et al. in 1993 and described in the next chapter.

Graphical methods are easy to use and for this reason are very popular in the quantification of PET images. No particular arrangement or number of compartments is assumed; only reversibility/irreversibility characteristics are required.

3.1 Patlak Method

The Patlak graphical method is a linear technique which has been widely used in dynamic PET data quantification to obtain a quite precise parameter that could be used as a "gold standard" for other analysis, for example to partially validate models thereafter described. On the one hand, it doesn't allow to estimate all kinetic parameters but only a macro one instead; on the other, a precise knowledge of compartmental structure is not necessary. Nevertheless some hypotheses have to be fulfilled:

- there must be only one irreversible compartment
- the tracer should leave reversible compartment through the irreversible one or plasma
- the tracer kinetic should be described by linear differential equations of the first order
- there should be a time T^* after which all reversible compartments are equilibrated with plasma.

The Patlak plot belongs to a group of graphical analysis techniques, whereby the measured TAC undergoes a transformation and is plotted against some sort of "normalized time". The Patlak plot is given by the expression

$$\frac{C_{tissue}}{C_p} = K\frac{\int_0^t C_p(\tau)d\tau}{C_p(t)} + V \tag{3.1}$$

This means that the measured PET activity is divided by plasma activity, and plotted at a "normalized time" (integral of input curve from injection divided by instantaneous plasma activity).

For systems with irreversible compartments this plot will result in a straight line after sufficient equilibration time. For the FDG model the slope represents the net uptake rate, while the intercept V is equal to $V_0 + V_b$ with the distribution volume V_0 of the reversible compartment and the fractional

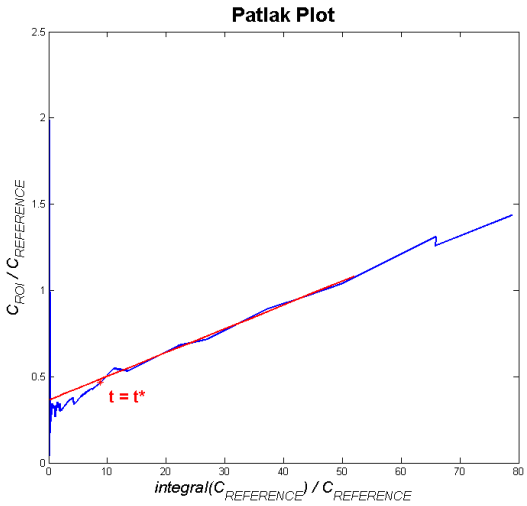

Figure 3.1: Example of Patlak plot

blood volume V_b. K value of equation 3.1 represents the regional metabolic glucose rate.

3.2 Compartmental Approach

Models used to quantify FDG kinetics have been developed and validated mostly to study solid organs such as brain, heart and liver.
During ALI there is the presence of healthy and injured tissue but no specific models for its description have been developed yet. Models already implemented for solid organs are not suitable for lungs because they have greater air content, lower basal glucose consumption, a larger perfusion to tissue ratio and a larger parenchymal edema and flooding to tissue ratio during organ injury.
A priori knowledge of compartmental structure is not available as well as the number of compartments necessary to describe tissue kinetic model. Availability of PET data together with plasma samples allows to fit compartmental models and obtain variable estimation related to tissue FDG transport and uptake. The following three compartmental models with an increasing number of compartments have been used to study pulmonary FDG kinetics

during ALI.

3.2.1 Two-compartment model: Patlak

Patlak et al. ([14]) proposed a model initially conceived to estimate cerebral glucose utilization. The model is composed of a central compartment in rapid equilibrium with blood plasma and a peripheral compartment in which the radiotracer is irreversible trapped.

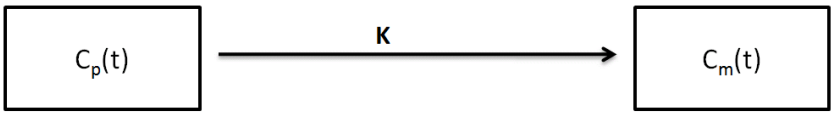

Figure 3.2: Generalized two-compartment (Patlak). The arrow indicates the directions of mass transport.

The main advantages of this model are the simple application and interpretation.
For what concerns lung tissue, the Patlak model has been applied by Jones et al.[10] and Bellani et al.[2]; each study proposes a normalization for the K constant. Jones normalized to tissue volume (V_e) to take into account the distribution volume of FDG in lung tissue; Bellani proposed to normalize by the mean fractional density of the lung, computed as (CT_{mean} + 1000(/1000, where CT_{mean} is the average CT number of the ROI. The implication of these normalizations are not well defined (e.g., they correct for the amount of tissue in the ROI, but it is unknown whether to take into account the lung edema). This uncertainty could be a limitation to the application of the Patlak model in ALI.

3.2.2 Three-compartment model: Sokoloff

Three-compartment model was originally conceived by Sokoloff et al. [17] and then used for PET [^{18}F]FDG studies in the brain and other organs/tissue. It shows blood and two tissue compartments, precursors and metabolic, and

together with the input-output experiment is described by

$$\dot{C}_e(t) = k_1 C_p(t) - (k_2 + k_3) \qquad C_e(0) = 0 \tag{3.2}$$

$$\dot{C}_m(t) = k_3 C_e(t) \qquad C_m(0) = 0 \tag{3.3}$$

Transfer constant rates characterize the transport between compartments:

- k_1 quantifies facilitated FDG transport from blood into the tissue (precursors compartment) per unit of tissue volume;
- k_2 quantifies tracer transport from the precursor compartment back into blood;
- k_3 characterizes FDG phosphorylation to ^{18}FDG-6-phosphate (metabolic compartment), which is assumed to be proportional to hexokinase activity.

Concentrations are so characterized: $C_p(t)$, [^{18}F]FDG plasma concentration; $C_e(t)$, [^{18}F]FDG tissue concentration; $C_m(t)$ [^{18}F]FDG-6-P tissue concentration. There's no equation for the first compartment $C_p(t)$ because in PET studies it is supposed to be known (from direct blood sampling or by extrapolation algorithm) and used for model identification. Blood activity curve is used as input function in model identification

$$C_b(t) = C_p(t)(1 - 0.3 * H) \tag{3.4}$$

where H is subject haematocrit.
From these compartments, a global measure of the fractional uptake (K) of [^{18}F]FDG and the distribution volume of the precursors compartment (F_e) as a fraction of lung volume can be computed:

$$K = k_1 * k_2/(k_2 + k_3) \tag{3.5}$$

$$F_e = k_1/(k_2 + k_3) \tag{3.6}$$

thus

$$K = F_e * k_3 \tag{3.7}$$

that is equivalent to the one computed with the Patlak method.

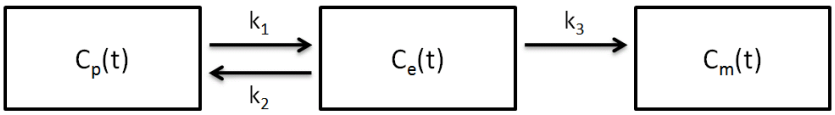

Figure 3.3: Three-compartment model. Arrows indicate the directions of mass transport.

The Sokoloff model includes the assumptions that after phosphorilation the radiotracer is irreversibly trapped into the tissue and that all extravascular unmetabolized FDG in the region of interest is present in a single compartment, immediately available for phosphorylation.
The application of the Sokoloff model to lung tissue may not be completely accurate for both healthy subjects and patients because blood-tissue FDG exchange does not follow the same dynamic of other tissues and large pools of edematous tissue can be functionally separated from cells trapping FDG. Therefore another compartment model for FDG kinetics during ALI has been developed.

3.2.3 Four-compartment model: TEC

Schroeder et al. [16] formulated a model of lung [^{18}F]FDG kinetics that includes an extravascular/noncellular compartment in addition to blood and parenchyma, representing a pool of [^{18}F]FDG that is not a direct precursor for phosphorylation. The tracer activity is considered as the sum of activities in four functional compartments; $C_p(t)$ and $C_m(t)$ are the same as the Sokoloff model (blood compartment and metabolite compartment) while, instead of only one compartment for [^{18}F]FDG tissue concentration, there is an additional one. Thus, it could be defined an extravascular compartment representing the concentration of [^{18}F]FDG that constitutes the precursor pool for phosphorylation to [^{18}F]FDG-6-P ($C_{ei}(t)$) and an extravascular/noncellular compartment, which accounts for the concentration of [^{18}F]FDG that is not an immediate precursor for phosphorylation ($C_{ee}(t)$).

- k_1 quantifies facilitated [^{18}F]FDG transport from blood into the tissue

- k_2 quantifies tracer transport from tissue back into blood
- k_3 is the rate of 18FFDG phosphorylation to [^{18}F]FDG-6-P
- k_5 e k_6 describe the activity concentration changes due to forward and backward [^{18}F]FDG transfer between the precursor compartment and the extravascular/ noncellular compartment.

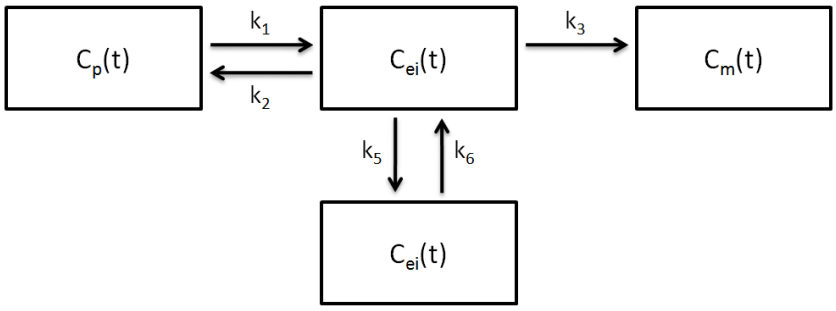

Figure 3.4: Lung-specific four-compartment model. Arrows indicate the directions of mass transport.

Chapter 4

Spectral Analysis

Spectral Analysis is an I/O model first implemented to determinate local metabolic rate of glucose in the brain [18], then commonly used with various PET tracers to study physiological systems such as liver, heart and kidney [7] and lately applied also to lungs.

4.1 Definition

Spectral Analysis (SA) is an input-output model to identify kinetic components of the tissue tracer activity without specific model assumptions, like the presence or absence of homogeneity in the tissue. This technique was introduced by Cunningham and Jones in 1993 [7] in order to determine local metabolic rate of glucose in the brain [18], but now SA is commonly used with various PET tracers to study physiological systems other than brain e.g. liver, heart, kidneys, etc... ([12];[13];[11]). In SA, the measure of the radioactivity in the tissue at the time t, $C_{tiss}(t)$, is modeled as a convolution of the plasma activity curve $C_p(t)$ with a sum of M + 1 distinct exponential terms:

$$C_{tiss} = \sum_{j=0}^{M} C_p(t) \otimes \alpha_j \cdot e^{-\beta_j t} \tag{4.1}$$

$$C_{tiss} = \sum_{j=0}^{M} \alpha_j \cdot \int_0^t C_p(\tau) e^{-\beta_j (t-\tau)} \tag{4.2}$$

where α_j and β_j ($\beta_1 < \beta_2 < ... < \beta_{M+1}$) are assumed positive or zero. This constraint derives from the assumption that the SA is modelling a first order compartmental system. The upper limit, M+1, represents the maximum numbers of terms to be included in the model and this is, in general, set to a large number to be established, usually 100. The values of β_j are predetermined and fixed in order to cover an appropriate spectral range. For the studies in vivo involving short lived positron emitting isotopes this range needs to extend to the slowest possible event of the tracer in the tissue up to a value appropriate to transient phenomena (e.g. the passage of activity through the tissue vasculature).

In general the corresponding term for $\lim\beta_j \to \infty$ (i.e. β_j with a very large value) is proportional to $C_p(t)$ via α_j , and can be seen as a "high-frequency" component. In the same way the corresponding term with a $\beta_j = 0$ or very close is proportional to $\int C_p(t)$ via α_j and can be viewed as a "low-frequency" component, i.e., accounting for the trapping of the tracer. Lastly, the components corresponding to the intermediate values β_j (intermediate frequency components) will reflect the uptake of the tracer within the tissue with their number corresponding to the number of identifiable tissue compartments within the ROI exchanging with plasma. This number is very important because it gives an indication of tissue heterogeneity. In light of these particular features ut is very common to define the SA model equation explicitly showing the trapping in the following way

$$C_{tiss}(t) = \alpha_0 \cdot \int_0^t C(\tau)d\tau + \sum_{j=1}^{M} \alpha_j \int_0^t C_p(\tau)e^{-\beta_j(t-\tau)}d\tau \tag{4.3}$$

When the βs values are given beforehand, the convolution integrals in the latter equation can be calculated using the input function. Then, the discrete form can be expressed by the following equations:

$$\begin{cases} C_{tiss}(t_1) = \alpha_1 \cdot f_1(\beta_1) + \alpha_2 \cdot f_1(\beta_2) + ... + \alpha_M \cdot f_1(\beta_M) \\ C_{tiss}(t_2) = \alpha_1 \cdot f_2(\beta_1) + \alpha_2 \cdot f_2(\beta_2) + ... + \alpha_M \cdot f_2(\beta_M) \\ \vdots \\ C_{tiss}(t_m) = \alpha_1 \cdot f_k(\beta_1) + \alpha_k \cdot f_k(\beta_2) + ... + \alpha_M \cdot f_k(\beta_M) \end{cases} \tag{4.4}$$

where k denotes the time index and $f_i(\beta_j) = \int_0^{t_i} C_p(\tau)e^{-\beta_j(t-\tau)}d\tau$. A system can be given in a matrix form where C contains $C_{tiss}(t_i)$, A contains α_j and M is the transfer matrix containing $f_i(\beta_j)$.

$$\overrightarrow{C} = \overrightarrow{M} \cdot \overrightarrow{A} \tag{4.5}$$

α value corresponding to each β can be easily obtained from equation 4.1 using the non-negative least squares method. In this study estimation operation has been done using the *lsqnonneg.m* function included in Matlab (Matlab R2009b, The Mathworks, Natick, MA) and a data weighted approach. The weight choice doesn't depend on the estimation algorithm but on the specific features of analyzed data. Precision of the $\alpha_j s$ is obtained from the inverse of the Fisher Information Matrix. When lim $\beta_j \to \infty$ (i.e. $beta_j$ with a very large value) the corresponding C_{tiss} term is proportional to Cp(t) via α_j, and can be viewed as a "high frequency" component, i.e., accounting for the fast passage of the tracer on the vascular space of the ROI. Contrariwise the corresponding term with $\beta_j \to 0$ is proportional to $\int_0^t C_p(\tau)d\tau$ via α_j and can be viewed as a "low frequency" component, i.e., accounting for a (quasi)trap for the tracer. The remaining components, corresponding to the intermediate values β_j ("intermediate frequency" components) will reflect the uptake of tracer within the tissue with their number corresponding to the number of distinct tissue compartments within the ROI exchanging with plasma. The number of intermediate components is very important because can give a clear idea of tissue heterogeneity.

4.1.1 Beta Grid definition

To implement the aforementioned model the first step was to define β_j's grid. Several distributions have been examined in previous studies, including linear, quadratic, logarithmic and a more common one suggested by DiStefano (1981) in which the range of β_j, j = 1,...., M was chosen as follows. The lower limit was $\beta_1 = (\frac{1}{3T_f})$, where T_f was the end time of experiment. The upper limit was $\beta_M = (\frac{3}{T_i})$ where T_i was the duration of the first scan. The

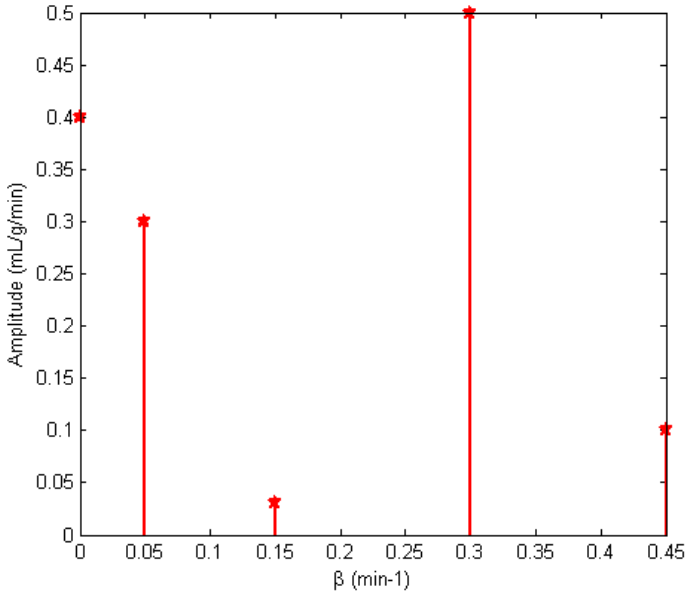

Figure 4.1: Example of a possible SA spectrum

spacing of the $\beta_j s$ was fixed as

$$\beta_j = \frac{1}{\tau_j}, \tau_j = \tau_{j-1} \left[\frac{T_f}{T_i}\right]^{[1/(M-1)]}, j = 1, ..., M \tag{4.6}$$

where M is the number of the points in the distribution. The components for $\beta_0 = 0$ and $\beta_{M+1} \to \infty$ were explicit included.

4.2 Features

SA spectra resulting from dynamic PET studies provide information about possible system behavior and could be correlated with a compartmental model approach. Although there are no priori assumptions, as to the number of components necessary to obtain optimal fits, the interpretation of α and β can lead to a definition of the best compartment model. Since the β values are discrete, the individual components of the spectra are generally comprised of one or two adjacent values for α. The sum of the α values within each component will subsequently be referred to as the com-

bined peak height for the component. Thus, a quite well defined spectrum is obtained, and a line-position based classification provides useful tools for model interpretation.

High-Frequency components close to or coincident with the upper level of the predefined range, could be generated by two sources. The first corresponds to the rapid transit time of tracer in the vasculature within the ROI. This is usually modeled as a constant blood volume term (V_b). It may be incorporated in the general linear model but the position of high frequency components, in contrast to those at lower frequencies, are very sensitive to the assumed delay between the arrival of arterial blood in the tissue ROI and in the online counter and for this reason it is better to treat the constant term as a high frequency. A second source relate to the dispersion of blood counts measured on $C_{tissue}(t)$ relative to the "true" arterial input $C_p(t)$ to the tissue ROI. High frequency terms have relatively little effect on the size and position of lower frequency components which relate to tissue retention and the subsequent release of tracer.

Intermediate and Low Frequency reflect the extravascular behavior of the tracer. The sum of these components plotted against time is the unit impulse response function of the extravascular tissue. The intercept at t=0 on the unit impulse response is the unidirectional clearance of tracer from plasma to tissue (given by the sum of the α), it is the product of the regional flow and extraction and in some cases it is an intrinsic part of the parameters of interest. The simplest interpretation of the number of components in the intermediate frequency range is that it corresponds with the number of reversible compartments of the tracer which can be discriminated in the tissue ROI. Multiple intermediate components may indicate tissue heterogeneity.

Lowest Frequency is coincident with, or close to, the limit set by the decay constant for the isotope and indicates the irreversible, or near irreversible trapping of the tracer. In the irreversible case the combined peak height of the low-frequency component gives the irreversible disposal rate constant of the tracer in blood or plasma (K, $ml \cdot sec^{-1} \cdot ml\ tissue^{-1}$), that is analogous to the Patlak K constant. This calculation is independent of the number of "reversible" components in the intermediate range of the spectrum.

4.3 Limitation

General SA algorithm shows some limitations such as low reliability in explaining data and underestimation of parameters. This is probably due to *a)* the presence of noise and errors in the input function signal; *b)* the trapping and the blood volume that could not be clearly detected; *c)* the presence of real equilibrating components of the system. Some of these factors may cause an uncorrected spectrum, e.g., the presence of double lines, really low-amplitude lines, higly-shifted lines. (Figure 4.2)
These limitations reduce the SA applicability especially when the data are particularly noisy.

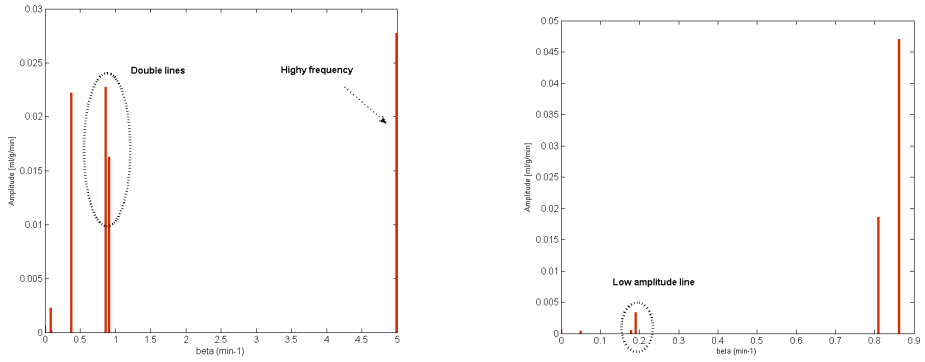

(a) Example of spectrum with double lines or really high frequency component

(b) Example of spectrum with small amplitude line

Figure 4.2: Examples of SA spectrum problems.

4.4 New Approach: SAIF

To overcome the limits of the traditional SA a new algorithm has been developed by Veronese et al.[19]: the Spectral Analysis Iterative Filter.
The SAIF algorithm conserves the main characteristics of SA but it is forced to operate the estimation of the net uptake rate constant in irreversible tracer. For this reason it may be an alternative quantification method for FDG PET studies.

4.4.1 Spectral Analysis Iterative Filter

A difficult operation for spectral analysis is to separate low- frequency equilibrating components from the trapping and also to separate high- frequency equilibrating components from blood.

The first part of SAIF consists in defining the beta grid (as in traditional spectral analysis) and set up the beta passband $[\beta_L, \beta_U]$; all components with $\beta \in [\beta_L, \beta_U]$ will be considered to be real equilibrating components of the system. The two iterative steps are as follows:

1. Components with β_i lower than β_L are assumed to result from the trapping components while those with $\beta_i > \beta U$ are shifted blood components. The components inside the passband are subtracted from the measured activity and the new values of the coefficient of the trapping compartment (α_0) and the blood volume fraction (V_b) are estimated.

2. Using the new values of α_0 and V_b, the contribution of trapping and blood components are subtracted from measured data. Using NNLS and the grid restricted to $\beta \in [\beta_L, \beta_U]$, the set of equilibrating components are re-estimated.

The stop criterion consists in calculating the difference between WRSS after the two steps; if it is less than $\epsilon = 0.001$ the iterative algorithm stops.

Beta Grid

The definition of beta grid should follow the general guidelines of SA but to be more consistent with the pathology study, it has been adapted to specific dataset.
A logarithmic distribution (base 10) with 100 elements from 0.1 to 5 has been chosen with an additional $\beta = 0$ term.

Cut-off values

The choice of the best beta passband in a crucial step of the filtering algorithm. Different cut-off values were tested for this specific study and

after looking at different resulting spectra, the following values were chosen: $\beta_L = 0.05$ and $\beta_U = 1$.

4.5 Compartmental Model and SA

In chapter 3 different compartmental models for the description of $[^{18}F]$FDG kinetics were illustrated. SA could be useful to define the model describing the tracer kinetics (Bertoldo et al. 1998 [3]); it provides information about the possible presence of trapping and the number of model compartments but it does not give information about how these compartments are connected to each other. Hereunder some examples are described to show the correlation in a simple way.

One-compartmental model

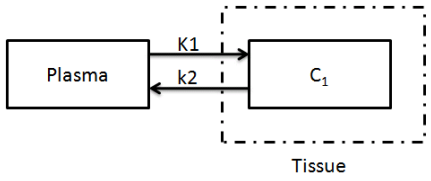

(a) A.Compartmental Model

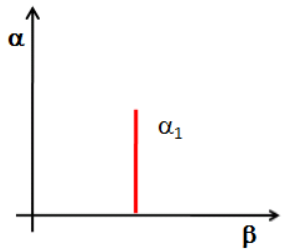

(b) A.Spectrum

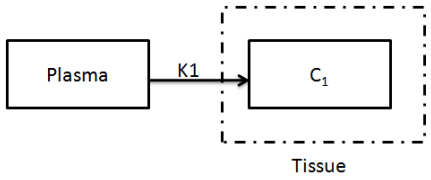

(c) B.Compartmental Model

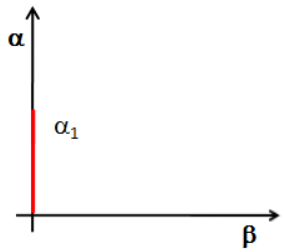

(d) B.Spectrum

Figure 4.3: One-compartmental model and relative spectrum.(a)(b) without trapping; (c)(d) presence of trapping.

In the first model K_1 and k_2 (Figure 4.3) correspond respectively to the

unidirectional clearance of tracer from blood to tissue and the rate constant for the transfer from tissue to blood. The corresponding SA spectrum shows only one component. The equations related to the model (Figure 4.3(a)) and the SA (Figure 4.3(a)) solutions are the following:

$$y(t) = K_1 \int_0^t C_p \cdot e^{-k_2(t-\tau)} d\tau \tag{4.7}$$

$$y(t) = \alpha \int_0^t C_p \cdot e^{-\beta(t-\tau)} d\tau \tag{4.8}$$

It is noticeable the equivalence between $K_1 \leftrightarrow \alpha$ and $k_2 \leftrightarrow \beta$. In the second model (Figure 4.3(c)(d)), where there is no transfer of the tracer from the tissue to the blood, i.e. $k_2 = 0$, the solution of the model is provided simply by the equations

$$y(t) = K_1 \int_0^t C_p d\tau \tag{4.9}$$

$$y(t) = \alpha \int_0^t C_p d\tau \tag{4.10}$$

This is typical when a trapping compartment is present . The corresponding spectrum still shows only one component but it is located at $\beta = 0$ and it is called *trapping component*; on the contrary, all components with $\beta \neq 0$ are called *equilibrating components* and are related to reversible components.

Two-compartmental model

In this example there is one more compartment which corresponds to an additional component in the spectrum. In the first case model and spectral analysis solution equations are:

$$y(t) = \frac{K_1 k_3}{k_2 + k_3} \int_0^t C_p(\tau) d\tau + \frac{K_1 k_2}{k_2 + k_3} \int_0^t C_p(\tau) \cdot e^{-(k_2+k_3)(t-\tau)} d\tau \tag{4.11}$$

$$y(t) = \alpha_0 \int_0^t C_p(\tau) d\tau + \alpha_1 \int_0^t C_p(\tau) \cdot e^{-\beta_1(t-\tau)} d\tau \tag{4.12}$$

In the second case there is an additional rate constant k_4 for the transfer

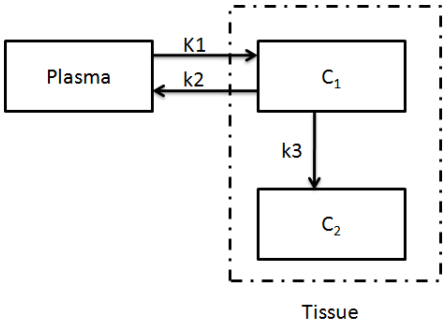

(a) A.Compartmental Model

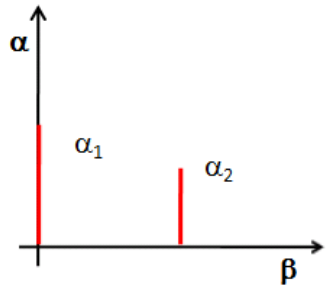

(b) A.Spectrum

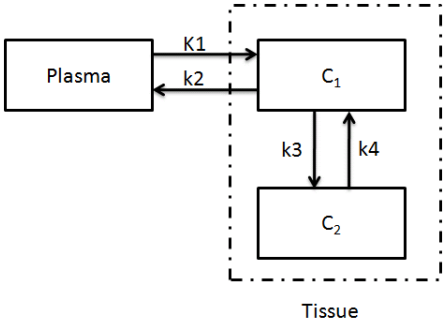

(c) B.Compartmental Model

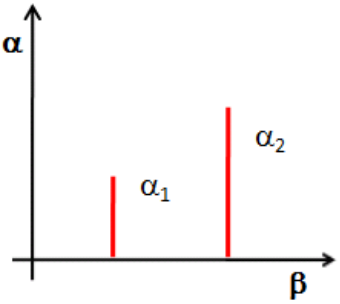

(d) B.Spectrum

Figure 4.4: Two-compartmental model and relative spectrum.(a)(b) presence of trapping; (c)(d) without trapping.

of the tracer from C_2 to C_1 and the corresponding spectrum shows a new equilibrating component instead of the trapping one.

Chapter 5

Results

In this chapter we are going to present the main results obtained from processing $[^{18}F]FDG$ data using the different analysis methods previously illustrated. Data were analyzed on the level of interest: Region Of Interest (ROI) level or voxel level.

5.1 Analysis at ROI level

Two different ROIs were defined according to the segmentation illustrated in section 2.3.2: Normally Aerated tissue (NA) and Collapsed/Consolidated tissue (CO).

Before the application of the quantification methods, ROI time-activity curves were obtained by average voxels time-activity curve within region. An example of this is reported in Figure 5.2.

All methods work with weighted data and weights are defined according to $w_i = \sqrt{\frac{\Delta Tscan_i}{Ctiss_i}}$. Where $\Delta Tscan_i$ is the length of i-esime scan (minutes) and $Ctiss_i$ is the total activity for the PET during i-esime scan.

5.1.1 Patlak Results

Patlak graphical method was applied according to what is described in section 3.1. The tissue time-activity curve and input function were used to obtain the Patlak plot and linearization was achieved starting on $t^* \simeq 7min$.

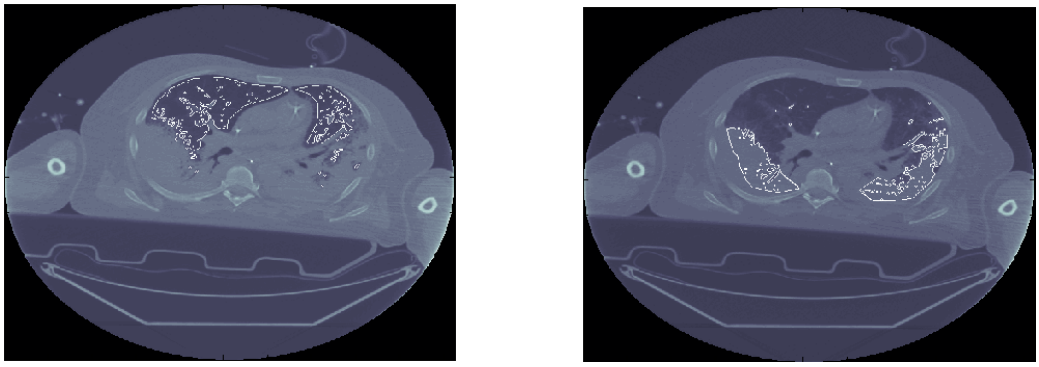

(a) Normally Aerated (b) Collapsed

Figure 5.1: CT images in one representative subject of two different ROI: normally aerated and collapsed.

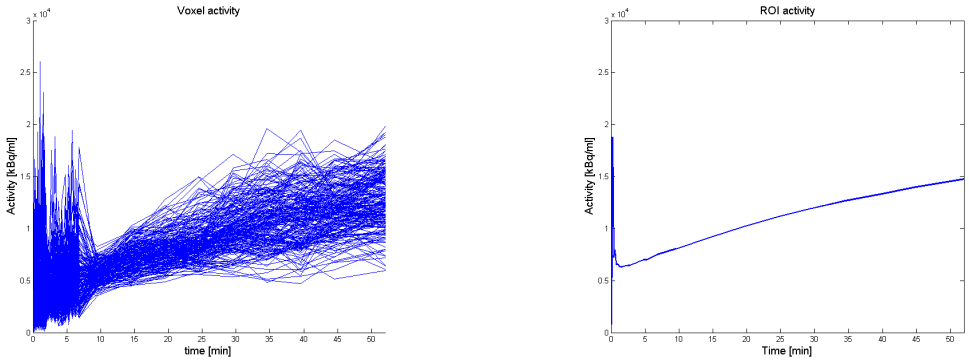

(a) Voxel activity (b) ROI acitivty

Figure 5.2: Tissue time-activity curve at voxel level and tissue level.

Individual estimate

Hereunder the K parameters obtained for the two groups of healthy subjects and patients are collected.

Three different situations are noticeable from Figure 5.3. Healthy subjects show low values for K [0.0002–0.0242 (ml/g/min)] in both normal and collapsed tissue. In regard to patients affected with ALI/ARDS two different behaviors could be distinguished; one group shows low K values for normal tissue and high values for the inflamed one, while the other group shows high K values for both normal and collapsed tissue. From now on patients of the

former group will be indicate as *coupled* while patients of the second group as *uncoupled*. These three different situations are reported in Figure 5.3.

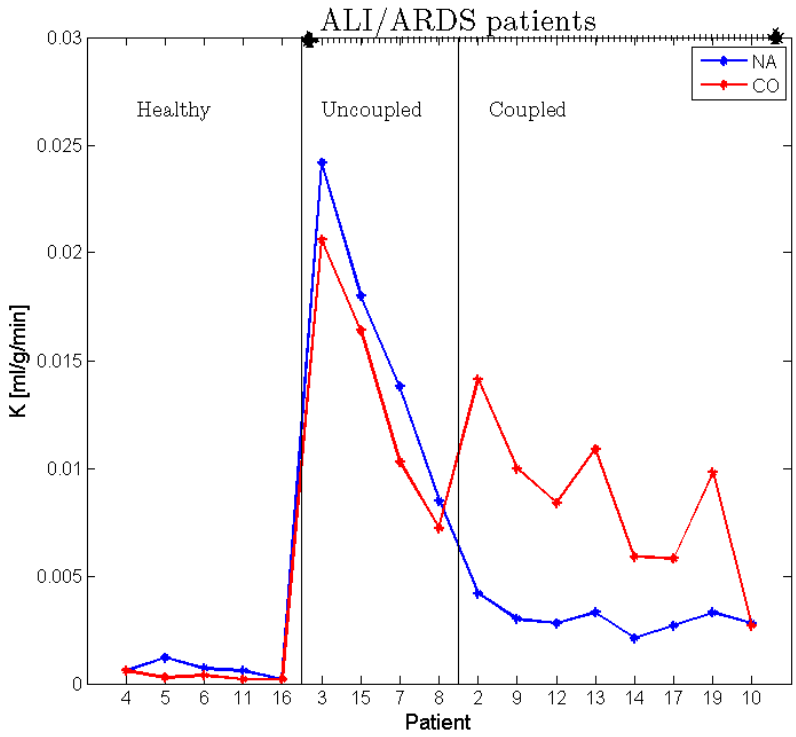

Figure 5.3: Patlak K estimate at ROI level.

Each group of subjects is characterized by different percentage of NA and CO tissue towards total tissue, in detail

Group	NA tissue (%)	CO tissue (%)
Healthy	>99	<1
Uncoupled	$\simeq$ 70	$\simeq$ 30
Coupled	$\simeq$ 80	$\simeq$ 20

Statistics

Individual estimations were used to obtain mean values for each group of patients and to apply the statistical t-test. Mean, standard deviation and

p-value (from t-test) are collected in Figure 5.4 and Table 5.1; in particular healthy subjects were compared to coupled and uncoupled.

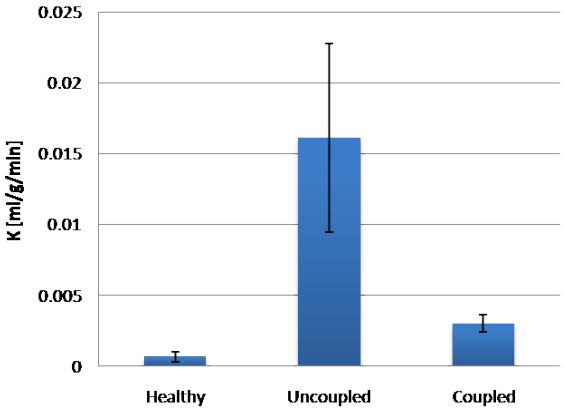

(a) Normally Aerated

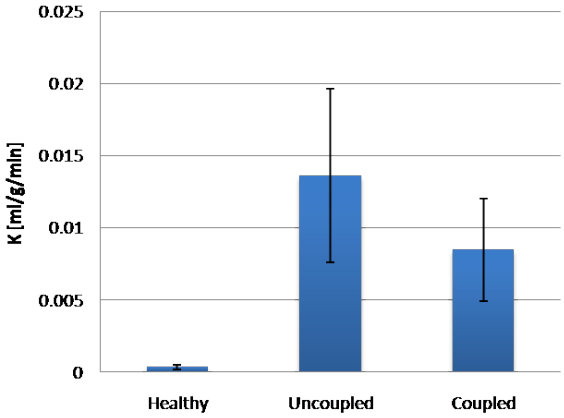

(b) Collapsed

Figure 5.4: Mean Patlak K estimate at ROI level between subjects of each group in NA and CO tissue.

From Figure 5.4 it is noticeable that healthy subjects provide really lower values of K estimate than patients affected with ALI; this is the natural consequence of inflammation that implies an increase in neutrophils activation. Compared to the previous paragraph the difference between *coupled* and *uncoupled* subjects is even clearer; the coupled show high activation only in consolidated tissue, the one that should be affected by inflammation, while the uncoupled show indiscriminately high activation.

(a) Normally Aerated

Group	K mean [ml/g/min]	SD [ml/g/min]	p value
Healthy	0.0007	0.0004	
Uncoupled	0.0161	0.0066	0.0011
Coupled	0.0030	0.0006	<0.0001

(b) Collapsed

Group	K mean [ml/g/min]	SD [ml/g/min]	p value
Healthy	0.0003	0.0002	
Uncoupled	0.0136	0.0060	0.0015
Coupled	0.0085	0.0036	0.0004

Table 5.1: Statistics of Patlak K estimates at ROI level in all the groups of subjects. t-test between healthy VS coupled and uncoupled patients was also performed.

5.1.2 SA Results

Spectral Analysis was applied according to what is described in section 4.1. SA was first implemented using the standard DiStefano distribution for the beta grid, then it was also implemented with a logarithmic distribution. As it can be seen from Figure 5.1.2, with DiStefano distribution high frequency components are more affected by V_b term and this behavior biases also the low frequency component estimation; the logarithmic distribution was for that selected.

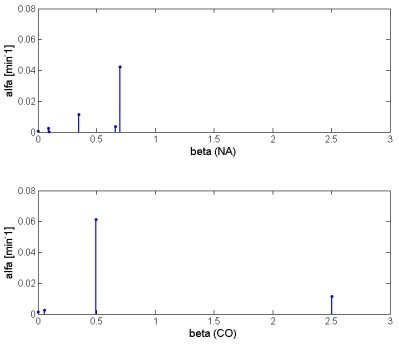

(a) Healthy - DiStefano

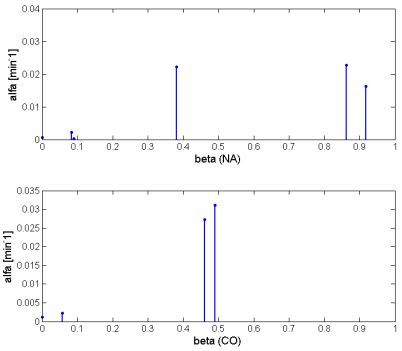

(b) Healthy - Logarithmic

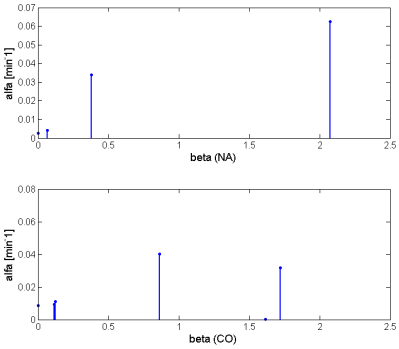

(c) Coupled - DiStefano

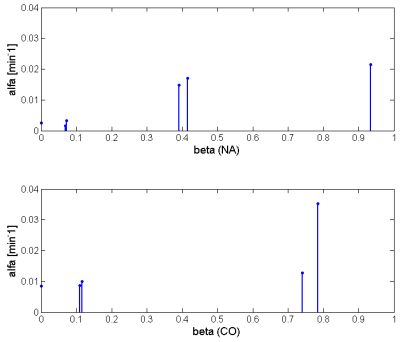

(d) Coupled - Logarithmic

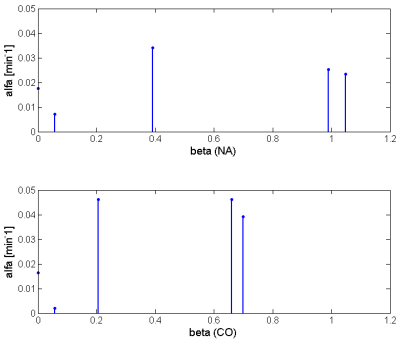

(e) Uncoupled - DiStefano

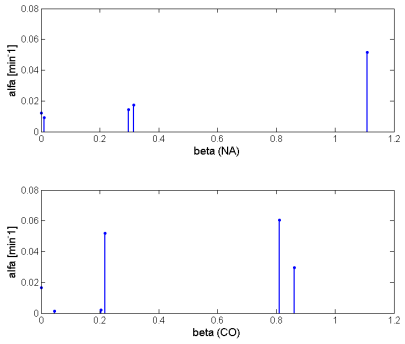

(f) Uncoupled - Logarithmic

Figure 5.5: Comparison of SA results of representative subjects with DiStefano and Logarithmic distribution for beta grid.

Model fit of the data

With parameters derived from the spectral analysis (α_i and β_i) an estimation of the time-activity curve could be obtained. The comparison of the model prediction time-activity curve with the major activity is useful to check the goodness of the results. Figure 5.6- 5.8 show some fit examples for NA and CO tissue of each group. Data are well fitted by the blue lines so spectral analysis seems to have high performance but looking at the next spectra, the situation does not seem so good. SA estimated spectra present some problems like the presence of double lines and components with amplitude very close to zero.

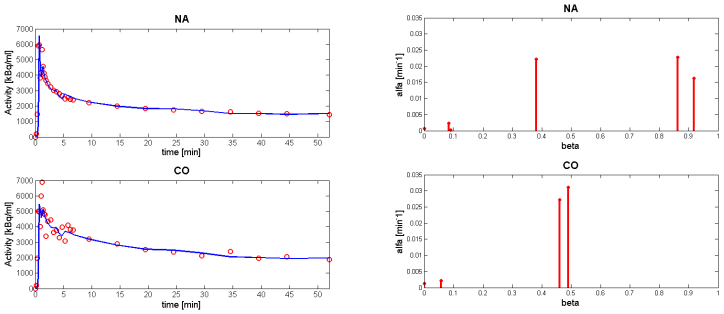

(a) Fit (b) Spectra

Figure 5.6: SA fit and spectra at ROI level in one representative healthy subject for NA and CO tissue.

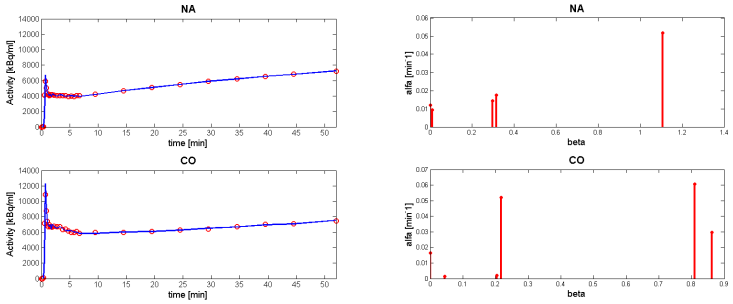

(a) Fit (b) Spectra

Figure 5.7: SA fit and spectra at ROI level in one representative uncoupled subject for NA and CO tissue.

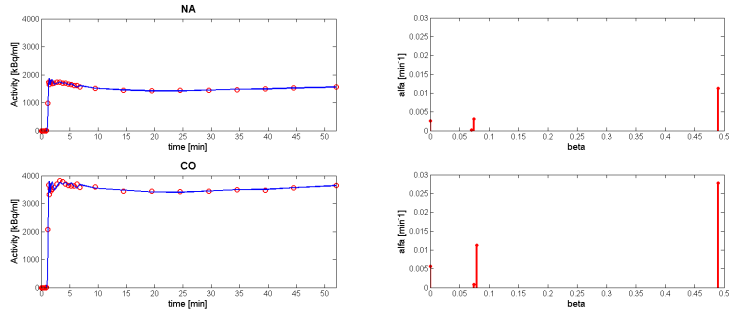

(a) Fit (b) Spectra

Figure 5.8: SA fit and spectra at ROI level in one representative coupled subject for NA and CO tissue.

Individual estimation

K estimates obtained from SA are here reported grouped in *healthy*, *coupled* and *uncoupled* as has been previously done with the Patlak results (Figure 5.3). Table 5.2 reports mean and standard deviation of SA K estimates performed in each group of subjects in NA and CO tissue. Figure 5.10 shows the correlation between the Patlak and Spectral Analysis K estimates performed at ROI level.

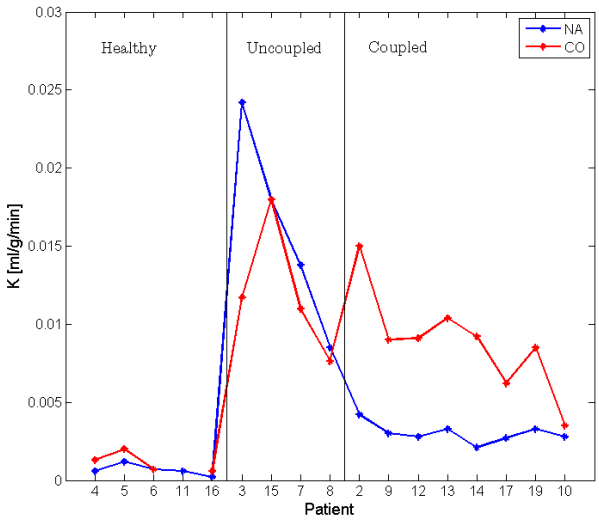

Figure 5.9: Mean SA K estimate at ROI level between subjects of each group in NA and CO tissue.

K estimates (Figure 5.10) have the same trend as the Patlak's and this correlation is even clearer from the scatter plot where the regression line has $slope = 0.8653$ and $intercept = 0.0007$.

(a) Normally Aerated

Group	K mean [ml/g/min]	SD [ml/g/min]
Healthy	0.0007	0.0004
Uncoupled	0.0161	0.0066
Coupled	0.0030	0.0006

(b) Collapsed

Group	K mean [ml/g/min]	SD [ml/g/min]
Healthy	0.0012	0.0006
Uncoupled	0.0121	0.0043
Coupled	0.0089	0.0033

Table 5.2: Statistics of SA K estimates at ROI level in all the groups of subjects.

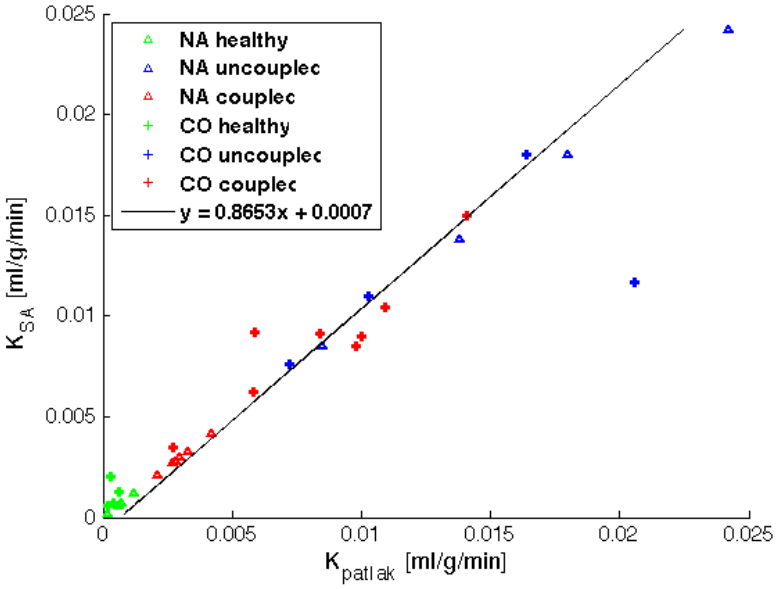

Figure 5.10: Scatter plot between the Patlak and SA estimate at ROI level. The regression line represents the correlation between two methods for the K estimation of all tissue type for all subjects.

Average spectrum

The average spectrum of each group were obtained after we had manually selected specific beta range. All the spectra of a specific group were visualized in one picture, then adjacent spectra lines were grouped and the corresponding beta range was fixed. The average spectrum was obtained by meaning α_s and β_s that relapsed in each range.

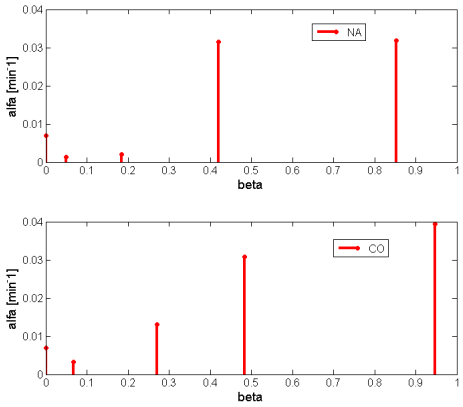

Figure 5.11: SA average spectra at ROI level of all healthy subjects.

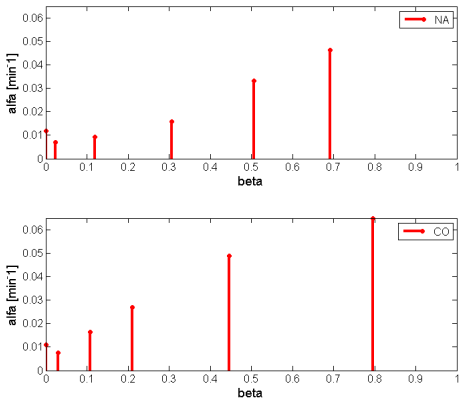

Figure 5.12: SA average spectra at ROI level of all uncoupled subjects.

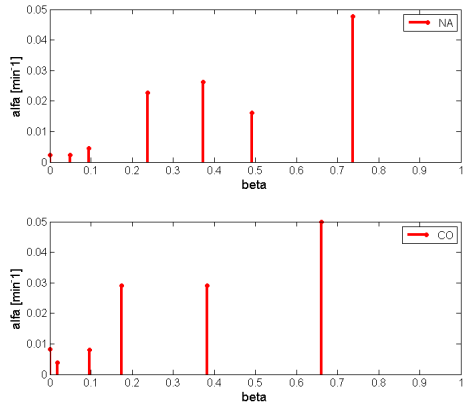

Figure 5.13: SA average spectra at ROI level of all coupled subjects.

In the examples of Figure 5.6-5.8 we had already noticed a very complex spectra situation; the same complexity is shown in the average spectra (Figure 5.11-5.13) where there are lines barely noticeable and several other lines. It is hard to deduce physiological relevant information from this situation; we need to "clean up" the spectrum from redundant lines with the filtered spectral analysis.

5.1.3 SAIF Results

Spectral Analysis Iterative Filter was applied according to what is described in section 4.4. In order to be consistent with SA results we applied the same logarithmic beta grid; we set a β passband filter interval of $[0.05 - 1](min^{-1})$ according to the results of standard spectral analysis.

Fit

SAIF provides fit as good as SA, moreover the quality of the resulting spectra are better; we cleaned the spectra from the double components and the small components due to noise. Some examples, one for each subject group, are reported in Figure 5.14-5.16.

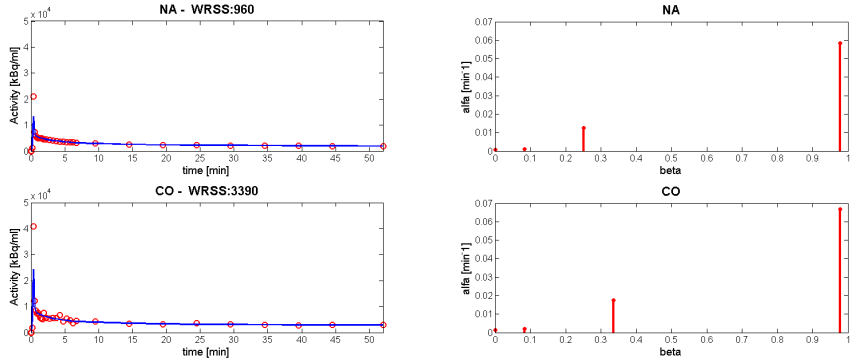

(a) Fit (b) Spectra

Figure 5.14: SAIF fit and spectra at ROI level in one representative healthy subject for NA and CO tissue.

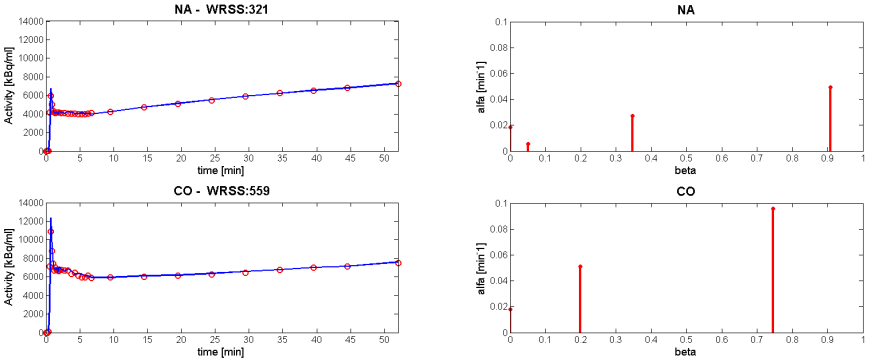

(a) Fit (b) Spectra

Figure 5.15: SAIF fit and spectra at ROI level in one representative uncoupled subject for NA and CO tissue.

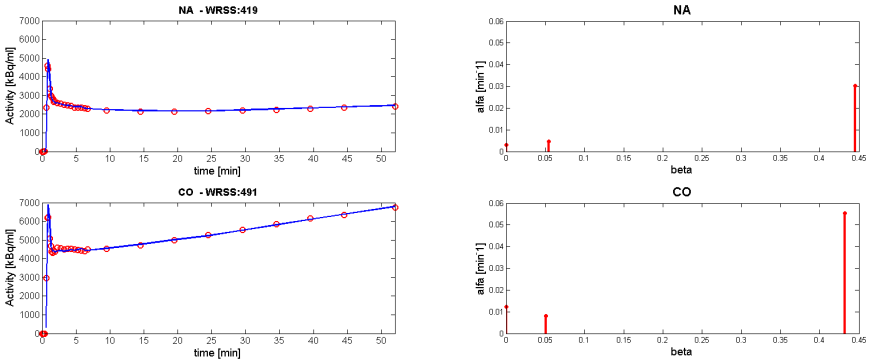

(a) Fit (b) Spectra

Figure 5.16: SA fit and spectra at ROI level in one representative coupled subject for NA and CO tissue.

Individual estimation

SAIF K estimate reported the same trend and subject classification of other methods; results are consistent with the Patlak K estimate (Figure 5.18).

(a) Normally Aerated

Group	K mean [ml/g/min]	SD [ml/g/min]
Healthy	0.0006	0.0004
Uncoupled	0.0160	0.0060
Coupled	0.0029	0.0006

(b) Collapsed

Group	K mean [ml/g/min]	SD [ml/g/min]
Healthy	0.0008	0.0005
Uncoupled	0.0151	0.0075
Coupled	0.0089	0.0037

Table 5.3: Statistics of SAIF K estimates at ROI level in all the groups of subjects.

When SAIF is compared with Patlak the correlation is better than standard SA as indicated in Figure 5.18. Here the regression line is characterized by $slope = 1.039$ and intercept very close to zero.

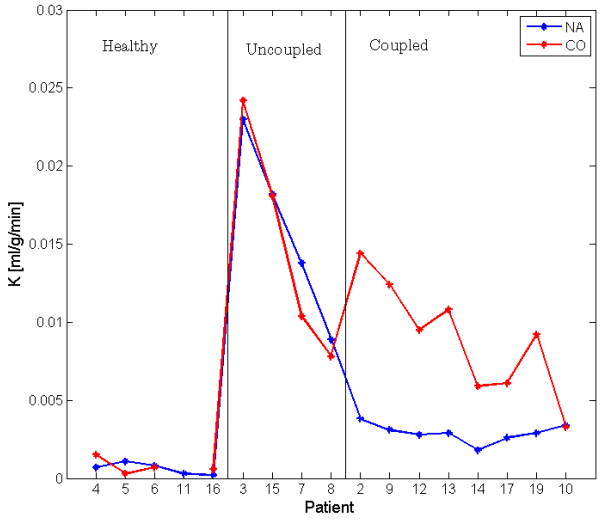

Figure 5.17: Mean SAIF K estimate at ROI level between subjects of each group in NA and CO tissue.

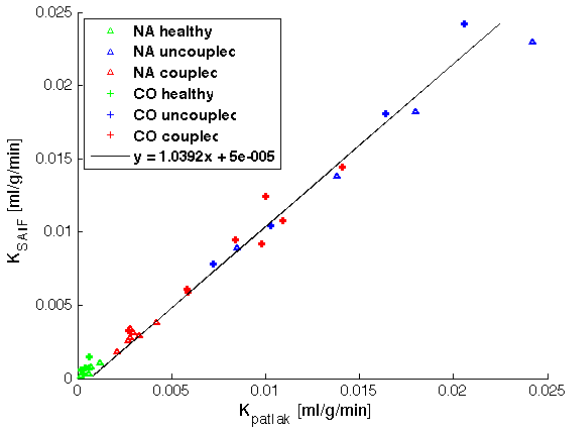

Figure 5.18: Scatter plot between Patlak and SAIF estimate at ROI level. The regression line represents the correlation between the two methods K estimate of all tissue types of all subjects.

Average spectrum

In order to obtain the average spectrum we operated in the same way as done for spectral analysis. For each group of subjects we visualized all the spectra together and grouped the lines with an adjacency criterion. Beta ranges are the same for each group: $range_1 = [0.01 \div 0.4]$ and $range_2 = [0.41 \div 0.9]$. The lines corresponding to $\beta > 0.91$ were not considered because probably due to V_b effect.

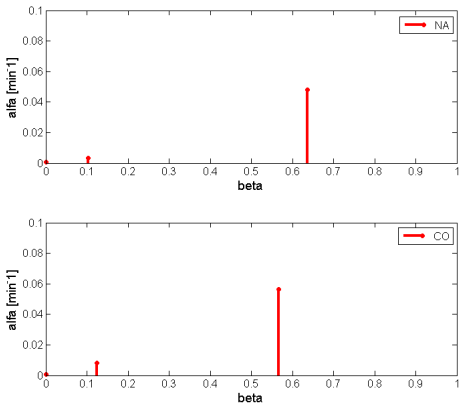

Figure 5.19: SAIF average spectra at ROI level of all healthy subjects.

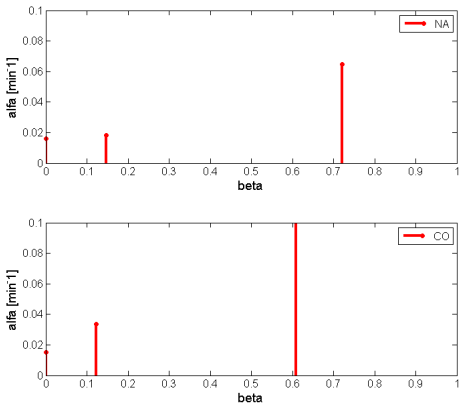

Figure 5.20: SAIF average spectra at ROI level of all uncoupled subjects.

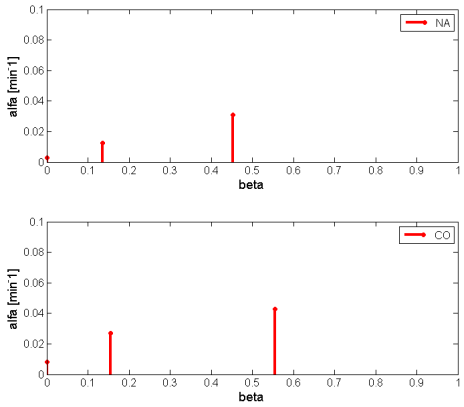

Figure 5.21: SAIF average spectra at ROI level of all coupled subjects.

All spectra have the same number of lines. There is always one line on $\beta = 0$ that corresponds to FDG trapping; in *healthy* subjects it is really small for both normally aerated and collapsed tissue. *Coupled* subjects shows a little more bigger *trapping line* for collapsed tissue while *uncoupled* have quite big lines for both tissue types. As regards the *equilibrating compartment lines*, there is always a small line in the first half of the spectrum and a bigger one in the second half. This may be due to different reasons:

Hp.1 lung tissue could be described by a three-compartmental model where, besides the trapping compartment, there are two additional equilibrating compartments: one with fast FDG exchange (line near zero) and one with slow exchange;

Hp.2 lung tissue could be described by a two-compartmental model and the additional third line is due to tissue heterogeneity.

More information is necessary to formulate the right hypothesis, for this reason we operated with a more precise voxel-based analysis.

5.2 Analysis at voxel level

In the previous section we operated considering all voxels within a ROI in order to obtain an estimation of the mean parameters that should describe

ROI's behaviors. This approach leads to rough results because does not take into account variability inside the region. For this reason we decided to run all the analysis voxel-by-voxel, to have a more accurate description of what is happening in all the lung parts and eventually to value the average parameters of a region of interest. The time-activity curve needed by the analysis methods is now the voxel's one (still weighted with $w_i = \sqrt{\frac{\Delta Tscan_i}{Ctiss_i}}$) while we used the same ROI's specifications such as beta grid, bounds etc.

5.2.1 Patlak Results

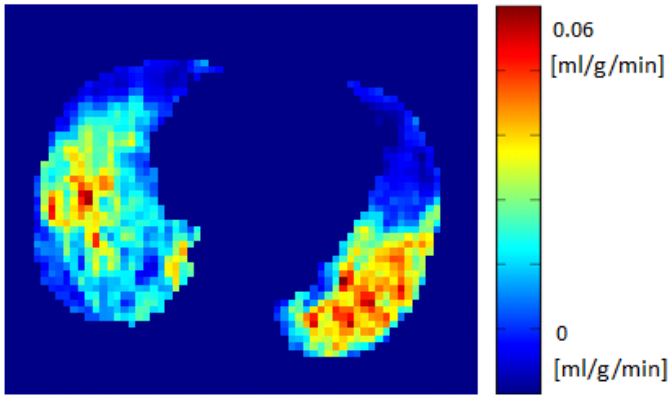

Figure 5.22: Parametric map of K estimate in one representative slice of one representative subject.

The application of the Patlak graphical method to all voxels results on a parametric map that shows areas with higher K values than others; these should correspond to areas with high activity and so inflamed lung tissue.

Individual estimation

Using the parametric map we calculated the average K value within a region of interest in order to compare the results with the ones obtained from the ROI approach. Even if the results are not the same, this is a common practice in PET literature to check the goodness of results. K estimate at voxel level (Figure 5.23) shows the same trend as the ROI one (Figure 5.3) and the distinction between *coupled* and *uncoupled* subjects is still clear.

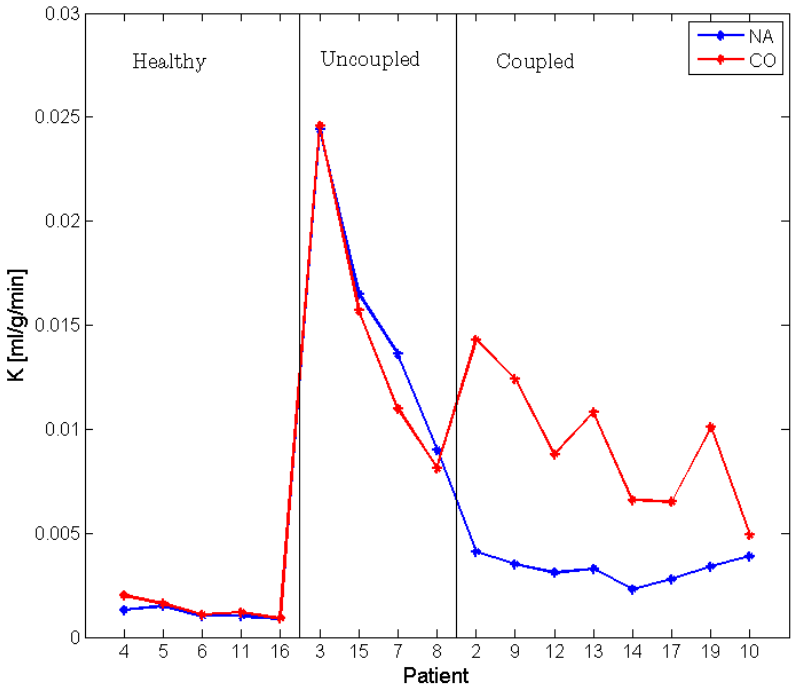

Figure 5.23: Mean Patlak K estimate at voxel level between subjects of each group in NA and CO tissue.

Statistics

Estimation of mean value of each group and statistical t-test results were obtained processing voxel's K values all together.

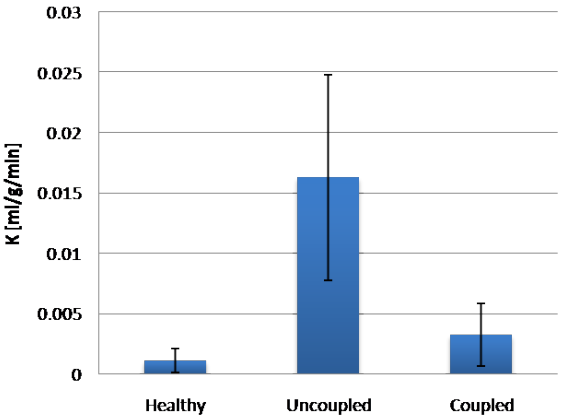

(a) Normally Aerated

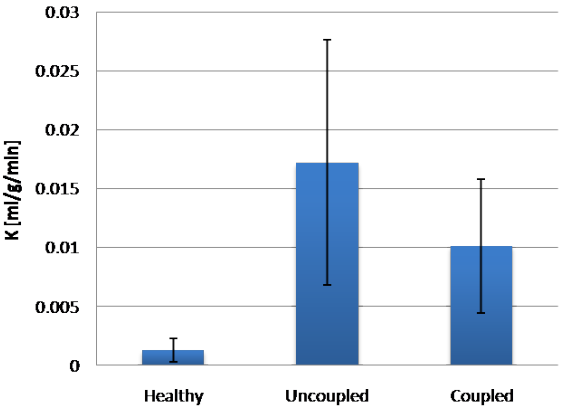

(b) Collapsed

Figure 5.24: Mean Patlak K estimate at voxel level between subjects of each group in NA and CO tissue.

(a) Normally Aerated

Group	K mean [ml/g/min]	SD [ml/g/min]	p value
Healthy	0.0010	0.0001	
Uncoupled	0.0160	0.0085	0
Coupled	0.0031	0.0027	0

(b) Collapsed

Group	K mean [ml/g/min]	SD [ml/g/min]	p value
Healthy	0.0014	0.0011	
Uncoupled	0.0166	0.0102	0
Coupled	0.0098	0.0067	0

Table 5.4: Statistics of Patlak K estimates at voxel level in all the groups of subjects. t-test between healthy VS coupled and uncoupled patients was also performed.

5.2.2 SAIF Results

We applied only the filtered spectral analysis and not the traditional one. With standard SA we did not obtain good results at ROI level so we foresaw to have bad results also at voxel level because of the increased noise.

Spectral analysis iterative filter was applied with the same beta grid and beta passband as the ROI approach. For each voxel we obtained a different spectrum and so a specific K estimate and a specific data fit.

Model fit of the data

Hereunder are collected some examples of SAIF spectra and respective data fit of two representative voxels (one for each tissue type) for every subject group.

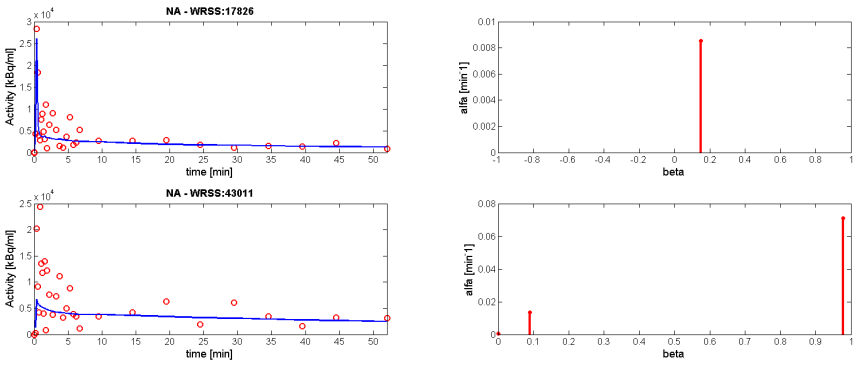

(a) Fit (b) Spectra

Figure 5.25: SAIF fit and spectra at voxel level in one representative healthy subject for NA and CO tissue.

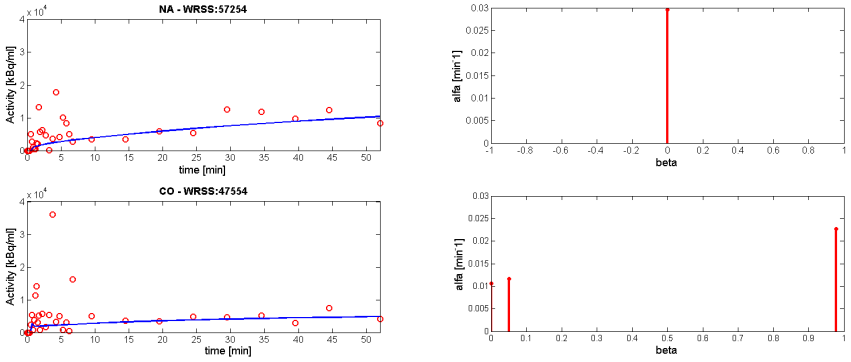

(a) Fit (b) Spectra

Figure 5.26: SAIF fit and spectra at voxel level in one representative uncoupled subject for NA and CO tissue.

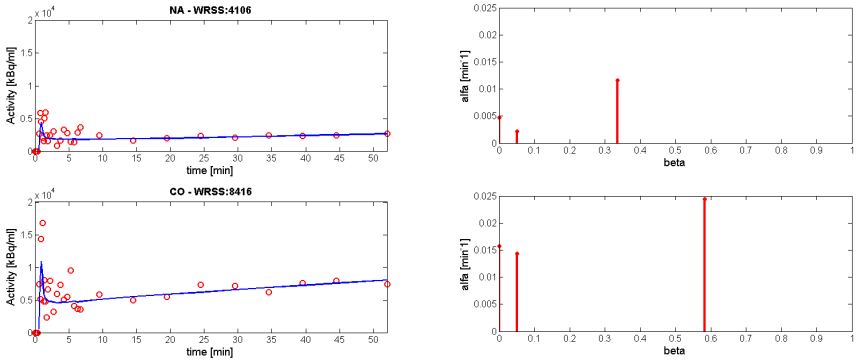

(a) Fit (b) Spectra

Figure 5.27: SAIF fit and spectra at voxel level in one representative coupled subject for NA and CO tissue.

The quality of the fit is consistent with the high level of noise of the data. In contrast with the ROI activity curve (Figure 5.14- 5.16), the voxel time-activity curves seem to be really noisy, particularly at early time. Spectra mostly show a three components behavior even though the first equilibrating component line is often really close to the trapping one or, as in *healthy* case, hasn't got a significant amplitude.

Individual estimation

Individual estimation for each subject was achieved by working out an average of voxel's K value; the new $K_{subject}$ were then used to calculate the global K_{mean} of each group.

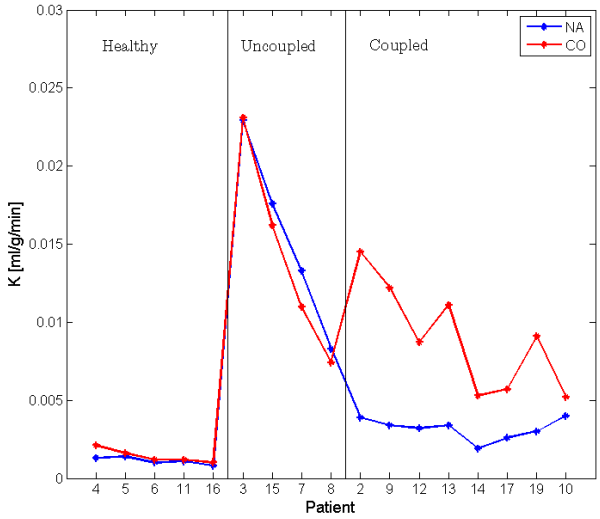

Figure 5.28: Mean SAIF K estimate at voxel level between subjects of each group in NA and CO tissue.

(a) Normally Aerated

Group	K mean [ml/g/min]	SD [ml/g/min]
Healthy	0.0006	0.0004
Uncoupled	0.0160	0.0060
Coupled	0.0029	0.0006

(b) Collapsed

Group	K mean [ml/g/min]	SD [ml/g/min]
Healthy	0.0008	0.0005
Uncoupled	0.0151	0.0075
Coupled	0.0089	0.0037

Table 5.5: Statistics of SAIF K estimates at voxel level in all the groups of subjects.

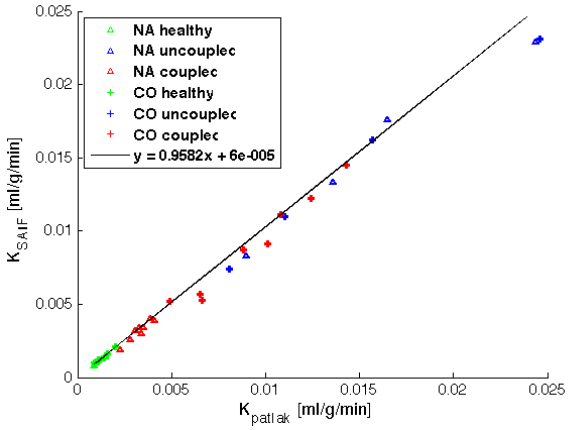

Figure 5.29: Scatter plot between Patlak and SAIF estimate at voxel level. The regression line represents the correlation between the two methods K estimate of all tissue types of all subjects.

Figure 5.29 shows a good correlation between the Patlak and SAIF voxel results. Then we defined 12 different regions on CT density basis and calculated each K_{mean} (Figure 5.30- 5.31). We can notice a good Patlak and SAIF correlation at detailed level as well as the more general NA and CO classification.

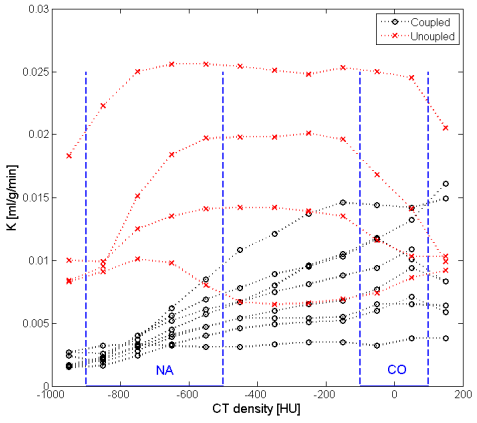

Figure 5.30: Patlak K estimate for coupled and uncoupled patients in 12 different density regions.

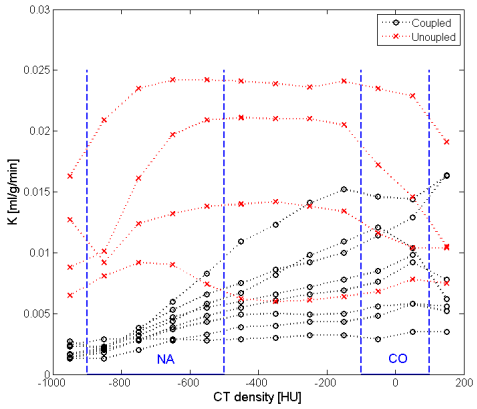

Figure 5.31: SAIF K estimate for coupled and uncoupled patients in 12 different density regions.

Components statistics

Since visual inspection of all voxels spectra would have taken too much time, we used an automated procedure to count spectrum lines and tried to prise out tissue model complexity. Figure 5.33 gives us important information about probable tissue kinetic model. Looking at the first two bar groups it is noticeable that only 20% of the total lung tissue has a spectrum with two equilibrating components while the majority shows a simpler model with only one component. If we go into detail we can notice the same trend for both aerated and collapsed tissue. This is why we think that the spectrum increased complexity is not due to an effective increase in the tissue model complexity but to tissue heterogeneity.

From Figure 5.34 we can perceive that voxels characterized by only one equilibrating component (that are about 80% of the total) have this component at low frequency while, voxels with two equilibrating components (about 20% of the total) do not show a specific pattern of distribution.

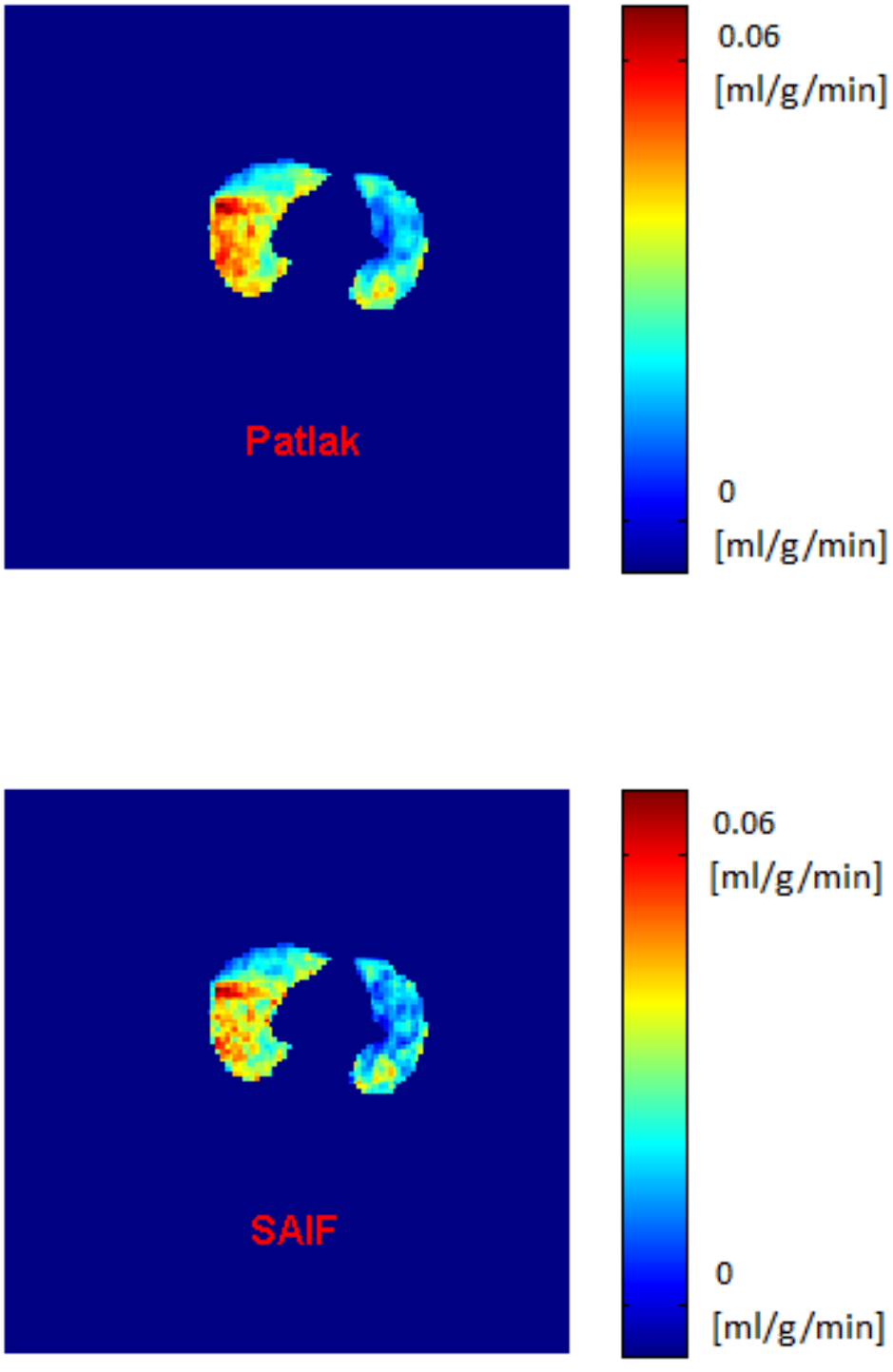

Figure 5.32: Parametric map of Patlak-K and SAIF-K estimate in one representative slice of one representative subject.

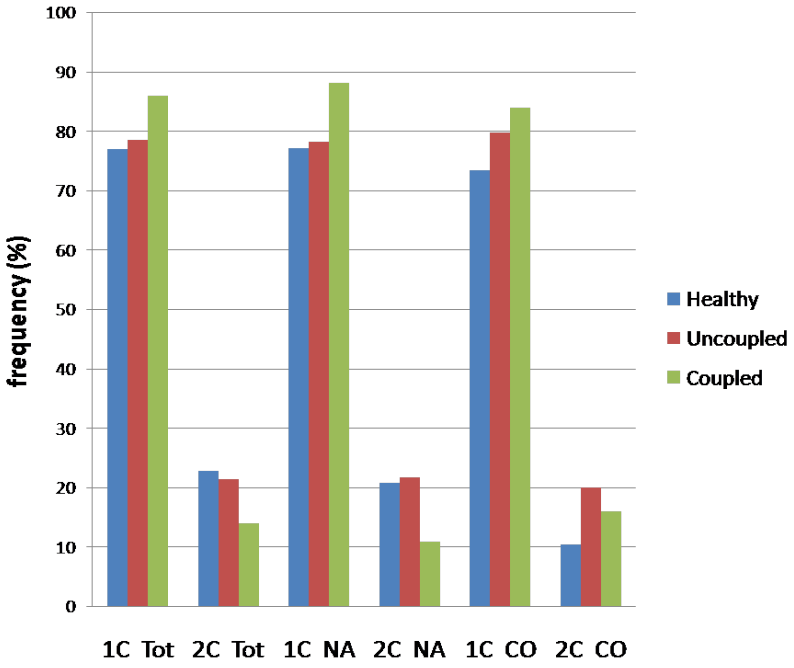

Figure 5.33: SAIF detected components incidence in different tissues. 1C refers to one equilibrating component; 2C refers to two equilibrating components.

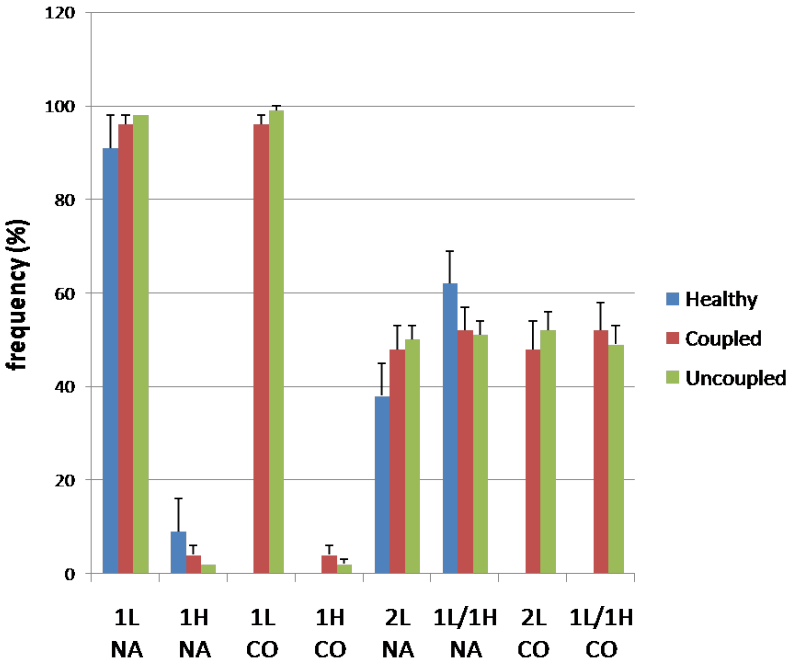

Figure 5.34: Distribution of SAIF voxel components at low and high frequency. 1L refers to one low component; 1H refers to one high component; 2L refers to two low components; 1L/1H refers to one low and one high components.

Spectrum examples

Figure 5.35 collects some spectrum examples of all possible situations. Each line refers to a different group of subjects: (a)(d) *healthy*; (e)(h) *uncoupled*; (i)(l) *coupled*. Every line shows, in order, two spectra for NA tissue (the first with only one component and the second with two components) and two spectra for CO tissue.

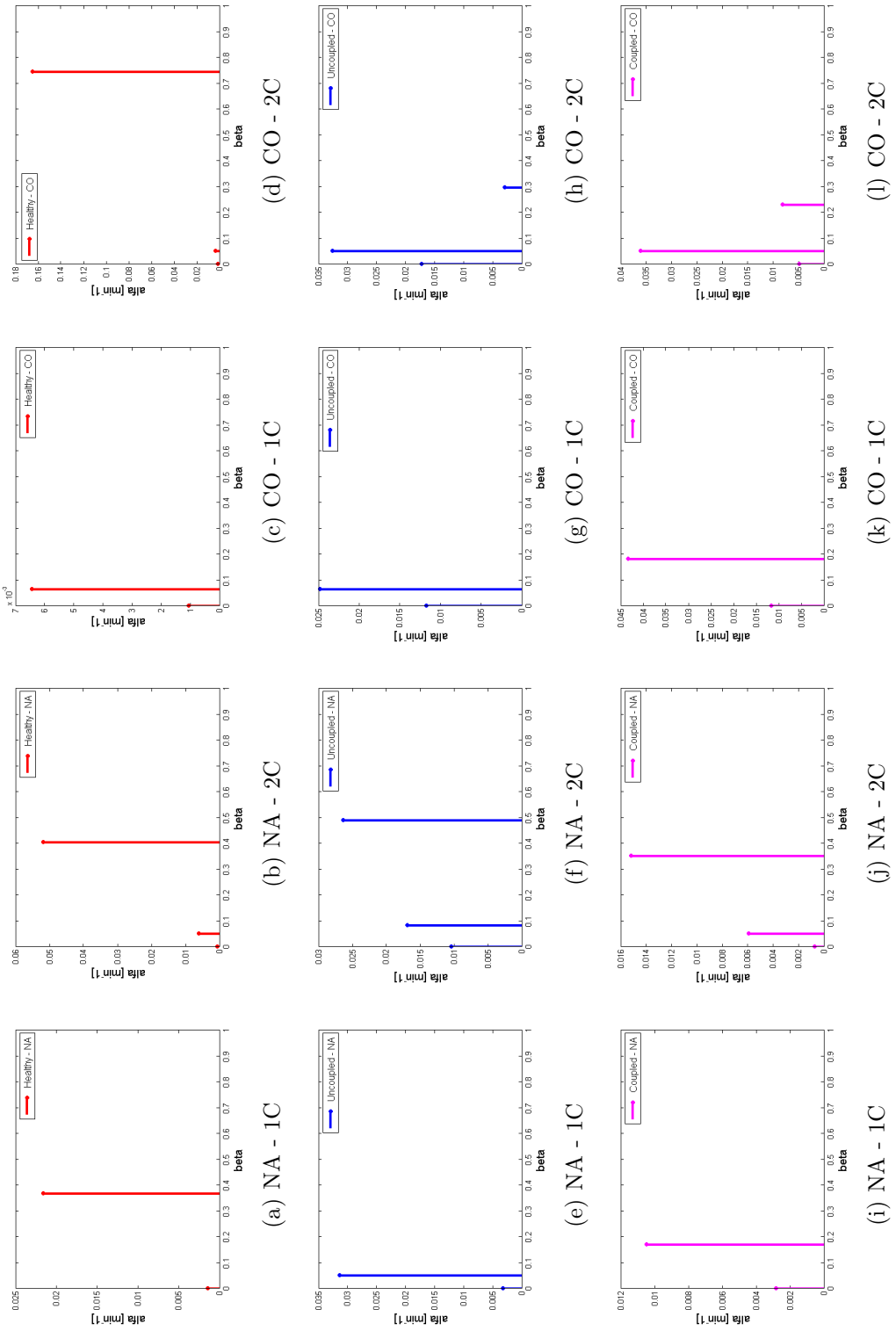

(a) NA - 1C (b) NA - 2C (c) CO - 1C (d) CO - 2C

(e) NA - 1C (f) NA - 2C (g) CO - 1C (h) CO - 2C

(i) NA - 1C (j) NA - 2C (k) CO - 1C (l) CO - 2C

Figure 5.35: SAIF-voxel spectrum examples.(a)(d) healthy subjects;(e)(h) uncoupled subjects;(i)(l) coupled subjects.

These examples strengthen the idea that there is a large heterogeneity among subjects and NA and CO tissue.

5.3 ROI vs Voxel

The results obtained from ROI-based and voxel-based analysis are consistent as regards K estimations whereas are not for spectrum constitution. The following pictures show the correlation between ROI and voxel analysis for each method.

Patlak

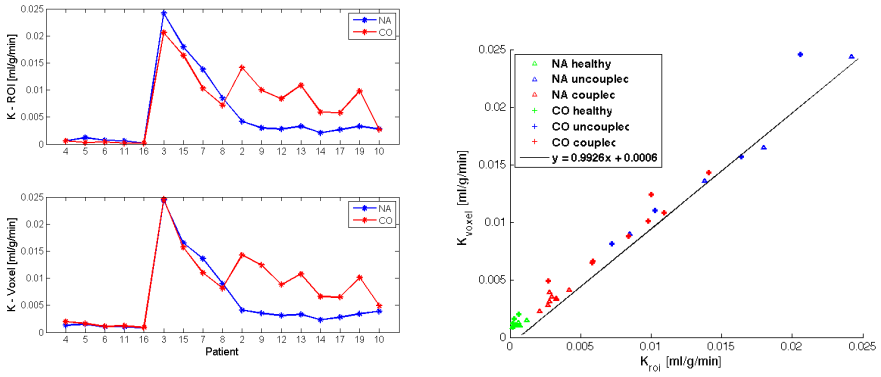

(a) K values (b) Correlation ROI-Voxel

Figure 5.36: Correlation of Patlak-K estimates obtained from ROI and voxel analyses

SAIF

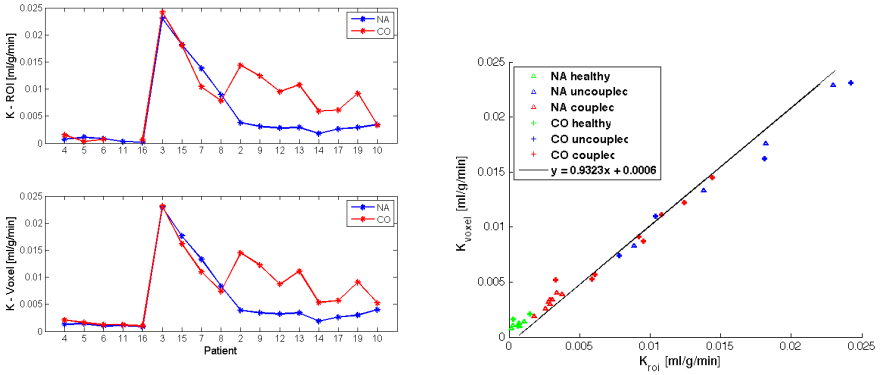

(a) K values (b) Correlation ROI-Voxel

Figure 5.37: Correlation of SAIF-K estimates obtained from ROI and voxel analyses

The advantage of a voxel-by-voxel analysis is to investigate tissue heterogeneity that still does not affect ROI mean estimates; this can be seen from the good correlations of Figure 5.36–5.37.

Chapter 6

Conclusion

In this work we applied the traditional [^{1}8F]FFDG PET quantification methods to patients affected with ALI. We first applied the Patlak graphical method, the Spectral Analysis and the Spectral Analysis Iterative Filter to two different regions of interest and thereafter to all voxels individually. The aim of the study was to verify the applicability of traditional PET quantification methods to lung tissue, not merely to solid organs, and to obtain physiological relevant information about the inflammation mechanism.

At the beginning we had to define the regions of interest and this was achieved through CT segmentation on the basis of considerations about the tissue density. Low CT density is characterized by normal alveolar distention typical of healthy and aerated tissues while high density tissues can show two different configurations: alveolar collapse typical of hypoxemia or normal alveolar distention with presence of tissue edema.
The Aapplication of the Patlak method to normally aerated and collapsed lung tissue, gave us important information about FDG tissue uptake. Healthy subjects showed low FDG uptake equally, while two different patterns were recognizable within patient group. A group of 7 patients showed higher uptake for collapsed tissue than the normally aerated while the remaining 5 patients showed high value of FDG uptake in both kinds of tissue. This was probably due to the presence of alveolar edema but more information was necessary to formulate a definitive hypothesis. In order to obtain hints about

kinetic description, we applied both spectral analysis and its filtered version but the latter provided better results so it was preferable.
We noticed that the estimation of SAIF parameters describing FDG uptake was well correlated with the Patlak results corroborating trustworthiness of subsequent SAIF estimations. This correlation was strengthened by the voxel-by-voxel analysis so we can conclude that the Patlak and SAIF methods can be successfully applied to solid organs and lung tissue as well.
Looking at SAIF spectra obtained by means of ROI analysis we could conjecture that FDG kinetic in lung tissue was described by a three compartmental model, however a second hypothesis could be made, i.e. spectra complexity was due to heterogeneity and so the actual model had just two compartments. The results obtained by the application of SAIF at voxel level seem to confirm the second hypothesis. Tissue heterogeneity does not seem to affect mean FDG uptake quantification, in fact, K estimates obtained with the ROI and voxel approach, correlate very well to each other.
In conclusion we can say that ALI patients have not homogeneous behavior, some of them show pathological characteristics in normally aerated tissues, and that is probably caused by differences in pathology seriousness. We can not propose a definitive model describing FDG kinetic in lung tissue; in fact, at ROI level a three compartmental one seems to be correct while the voxel analysis seems to prove the existence of a two compartment behavior. This difference could be due to tissue heterogeneity but further investigations are necessary.

Bibliography

[1] G. Bellani, L. Guerra, G. Musch, A. Zanella, N. Patroniti, T. Mauri, C. Messa, and A. Pesenti. Lung Regional Metabolic Activity and Gas Volume Changes Induced by Tidal Ventilation in Patients with Acute Lung Injury. *Am J Respir Crit Care Med*, 183(9):1193–99, 2011.

[2] G. Bellani, C. Messa, L. Guerra, E. Spagnoli, G. Foti, N. Patroniti, R. Fumagalli, G. Musch, F. Fazio, and A. Pesenti. Lungs of patients with acute respiratory distress syndrome show diffuse inflammation in normally aerated regions: A [^{18}F]-fluoro-2-deoxy-D-glucose PET/CT study. *Crit Care Med*, 37(7):2216–22, 2009.

[3] A. Bertoldo, P. Vicini, G. Sambuceti, A. A. Lammertsma, O. Parodi, and C. Cobelli. Evaluation of Compartmental and Spectral Analysis Models of $[^{18}F]FDG$ Kinetics for Heart and Brain Studies with PET. *IEEE Trans Biomed Eng*, 45(12):1429–48, 1998.

[4] P. Blake, B. Johnson, and J. VanMeter. Positron Emission Tomography (PET) and Single Photon Emission Computed Tomography (SPECT): Clinical Applications. *J Neuro-Ophthalmol*, 23(1):34–41, 2003.

[5] E. Carson and C. Cobelli. *Modelling Methodology for Physiology and Medicine.* Academic Press, 2000.

[6] C. Cobelli and R. Bonadonna. *Bioingengeria dei sistemi metabolici.* Pàtron Editore, 1998.

[7] V. J. Cunningham and T. Jones. Spectral Analysis of Dynamic PET Studies. *J Cerebr Blood Flow Metab*, 13(1):15–23, 1993.

[8] N. de Prost, M. R. Tucci, and M. F. Vidal Melo. Assessment of Lung Inflammation With $^{18}F - FDG$ PET during Acute Lung Injury. *AJR Am J Roentgenol*, 195(2):292–300, 2010.

[9] L. Gattinoni and A. Pesenti. The concept of "baby lung". *Intensive Care Med*, 31(6):776–784, 2005.

[10] H. A. Jones, S. Sriskandan, and A. M. Peters. Dissociation of neutrophil emigration and metabolic activity in lobar pneumonia and bronchiectasis. *Eur Respir J*, 10:795–803, 1997.

[11] K. Murase. Spectral analysis: principle and clinical applications. *Ann Nucl Med*, 17(6):427–34, 2003.

[12] K. Murase, T. Tsuda, T. Mochizuki, and J. Ikezoe. Spectral analysis applied to hepatobiliary dynamic scintigraphy with 99Tcm-N-pyridoxyl-5-methyltryptophan. *Nucl Med Commun*, 18(11):1049–56, 1997.

[13] K. Murase, T. Tsuda, T. Mochizuki, and J. Ikezoe. Hepatic extraction fraction of hepatobiliary radiopharmaceuticals measured using spectral analysis. *Nucl Med Commun,*, 20(11):1041–5, 1999.

[14] C. S. Patlak, R. G. Blasberg, and J. D. Fenstermacher. Graphical evaluation of blood-to-brain transfer constants from multiple-time uptake data. *J Cereb Blood Flow Metab*, 3:1–7, 1983.

[15] M. E. Phelps. Positron emission tomography provides molecular imaging of biological processes. *Proceedings of the National Academy of Science*, 97(16):9226–233, 2000.

[16] T. Schroeder, F. MArcos, M. D. Vidal Melo, G. Musch, S. Harris, J. G. Venegas, and T. Winkler. Modeling pulmonary kinetics of 2-deoxy-2-[^{18}F]fluoro-D-glucose during Acute Lung Injury. *Acad Radiol*, 15(6):763–75, 2008.

[17] L. Sokoloff, M. Reivich, C. Kennedy, M. H. Des Rosiers, C. S. Patlak, K. D. Pettigrew, O. Sakuarda, and M. Shinohara. The [^{14}C]deoxyglucose

method for the measurement of local cerebral glucose utilization: theory, procedure, and normal values in the conscious and anesthetized albino rat. *J Neurochem*, 28(5):897–916, 1977.

[18] F. Turkheimer, R. M. Moresco, G. Lucignani, L. Sokoloff, F. Fazio, and K. Schmidt. The use of spectral analysis to determine regional cerebral glucose utilization with positron emission tomography and [^{18}F]fluorodeoxyglucose:theory, implementation, and optimization procedures. *J Cereb Blood Flow Metab*, 14(3):406–22, 1994.

[19] M. Veronese, A. Bertoldo, S. Bishu, A. Unterman, G. Tomasi, C. B. Smith, and K. C. Schmidt. A spectral analysis approach for determination of regional rates of cerebral protein synthesis with the $L[1^{11}C]$leucine PET method. *J Cereb Blood Flow Metab*, 30(8):1460–76, 2010.

[20] A. P. Wheeler and G. R. Bernard. Acute lung injury and the acute respiratory distress syndrome: a clinical review. *Lancet*, 369:1553–64, 2007.

Acknowledgment

I would like to express my gratitude to my professor Alessandra Bertoldo for what she taught me and for the chance I had to work on this resarch with the collaboration of San Raffaele Insitute and the CNR. I thank Dr. Rosa Maria Moresco for her assistance during all my work and Dr. Giacomo Bellani for his helpfulness. I thank also the other members of IBFM institute for their welcome and kindness. Finally I would like to thank Mattia for his invaluable advice and for supporting me during the last month. Thanks to everyone that has contributed to the realization of this thesis.